



# **BROADBAND PUMPING EFFECTS ON THE DIODE PUMPED ALKALI LASER**

THESIS

Paul Nathaniel Jones, Civilian

AFIT/GAP/ENP/11-M04

DEPARTMENT OF THE AIR FORCE  
AIR UNIVERSITY

**AIR FORCE INSTITUTE OF TECHNOLOGY**

Wright-Patterson Air Force Base, Ohio

APPROVED FOR PUBLIC RELEASE; DISTRIBUTION IS UNLIMITED

The views expressed in this thesis are those of the author and do not reflect the official policy or position of the United States Air Force, The Department of Defense, or the United States Government. This material is declared the work of the U.S. Government and is not subject to copyright protection in the United States.

AFIT/GAP/ENP/11-M04

**BROADBAND PUMPING EFFECTS ON THE DIODE PUMPED  
ALKALI LASER**

**THESIS**

Presented to the Faculty

Department of Engineering Physics

Graduate School of Engineering and Management

Air Force Institute of Technology

Air University

Air Education and Training Command

In Partial Fulfillment of the Requirements for the

Degree of Master of Science in Applied Physics

Paul Nathaniel Jones, BS  
Staff Scientist, AFIT

March 2011

APPROVED FOR PUBLIC RELEASE; DISTRIBUTION UNLIMITED.

AFIT/GAP/ENP/11-M04

BROADBAND PUMPING EFFECTS ON THE DIODE PUMPED ALKALI LASER

Paul Nathaniel Jones, B.S.  
Civilian

Approved:

\_\_\_\_\_  
//signed//  
Glen P. Perram, PhD (Chairman)

\_\_\_\_\_  
Date

\_\_\_\_\_  
//signed//  
Lt. Col Jeremy C. Holtgrave (Member)

\_\_\_\_\_  
Date

\_\_\_\_\_  
//signed//  
Maj. Clifford Sulham (Member)

\_\_\_\_\_  
Date

## **Abstract**

This research seeks to gain greater insight on the mechanics of The Diode Pumped Alkali Laser through analytic modeling techniques. This work is an extension to a previous model developed by Dr. Gordon Hager, and focuses on the addition of pump-beam bandwidth. Specifically, it seeks to determine the effect that broadband pumping has on laser performance. The model incorporates all the fundamental parameters within the laser system, including alkali concentrations, collision partner concentrations, pump bandwidth, length and temperature of gain medium, transmission, and reflectivity. Baseline operating conditions set Rubidium (Rb) concentrations ranging from  $10^{12}$  -  $10^{14}$  atoms/cm<sup>3</sup>, corresponding to operating temperatures ranging from 50 – 150 C. Ethane or Methane concentrations are varied corresponding to partial pressures from 100 – 500 Torr. The system is evaluated for incident beam intensity ranging from 0 – 30000 W/cm<sup>2</sup>, for both lasing and non-lasing system analysis. Output laser beam intensities scale well with input beam intensity and the model predicts optical to optical efficiencies of over 70%.

AFIT/GAP/ENP/11-M04

*To The Air Force Institute of Technology*

## **Acknowledgments**

This work is the culmination of the efforts made by the faculty and staff of The Air Force Institute of Technology. Of greatest influence was my mentor, Dr. Glen Perram. His expertise, guidance, and patience created an environment where ideas were sparked, obstacles were overcome, and progress was made. Second I would like to thank Greg Smith and Michael Ranft. Their technical expertise and willingness to help enabled me to make timely progress on my experiments. Finally, I would like to thank three of my fellow graduate students, Greg Pitz, Cliff Sulham, and Matt Lange. Greg and Matt welcomed me into AFIT in a very professional and helpful way and made my transition into graduate school a success. Cliff was a true co-worker to me, and was someone I could bounce ideas off of, get advice on experiments, and rely on for the many small favors we experimenters ask of each other. Thank you.

Paul N. Jones

## Table of Contents

	Page
Abstract.....	iv
Acknowledgements.....	v
List of Figures.....	viii
List of Tables.....	xi
List of Symbols.....	x
I. Introduction.....	1
Background.....	1
The Diode Pumped Alkali Laser.....	2
Analytic Modeling.....	4
II. Literature Review.....	6
Alkali Earth Metals.....	6
Diode Pumped Alkali Laser Technology.....	16
III. Methodology.....	21
Introduction.....	21
Longitudinally Averaged Two-Way Intra-Cavity Pump Beam Intensity.....	24
Laser Rate Equations.....	26
Transcendental Solution.....	27
Frequency Dependence of the Pump Transition.....	29
IV. Results and Analysis.....	33
Introduction.....	33
Single Frequency, No Lasing Results.....	34
Single Frequency, Lasing Mode Results.....	35
Broadband Pump, Lasing Mode Results.....	41
V. Conclusions and Discussion.....	55
Appendix A. Rubidium Spectroscopic Data.....	59
Appendix B. Mathematica Code .....	60
Bibliography.....	80



## List of Figures

Figure	Page
1. DPAL Three Level Diagram (Rb).....	3
2. Rb D <sub>2</sub> Hyperfine Structure.....	9
3. Initial Population Inversion vs. Alkali Temperature.....	12
4. Rb Vapor Pressure vs. Temperature.....	14
5. Atmospheric Transmittivity.....	15
6. Standard DPAL configuration.....	18
7. Copper Waveguide Model and Results.....	19
8. Model Dependent Variables.....	22
9. Round Trip Pump Beam Intensity.....	24
10. Transcendental Intersection.....	28
11. $\Omega$ vs $I_{pin}$ .....	29
12. D1 Spectral Overlap.....	30
13. Steady State Alkali Concentrations – Pre lasing.....	34
14. Pre-Lasing Intracavity Pump Beam Intensity – Frequency Independent.....	35
15. Intracavity Laser Intensity – Frequency Independent.....	36
16. Intracavity Pump Intensity – Frequency Independent.....	37
17. Ethane Variation – Frequency Independent.....	38
18. Rubidium Variation – Frequency Independent.....	39
19. Transmittivity Variation – Frequency Independent.....	40
20. Cell Length Variation – Frequency Independent.....	41
21. $\Omega$ vs $I_{pin}$ – Frequency Dependent.....	42

Figure	Page
22. $I_{lase}$ vs $I_{pin}$ – Frequency Dependent.....	44
23. Ethane Variation – Frequency Dependent (19.73 GHz).....	44
24. Ethane Variation – Frequency Dependent (200 GHz).....	44
25. Reflectivity Variation – Frequency Dependent.....	45
26. $\Delta$ -Bandwidth Variation – Frequency Dependent.....	46
27. Reflectivity Variation 3D – Frequency Dependent.....	47
28. DPAL Efficiency – Frequency Dependent.....	48
29. Reflectivity Variation 2D – Frequency Dependent.....	49
30. DPAL Efficiency – Frequency Dependent.....	50
31. Gamma – 300 Torr Ethane.....	51
32. Gamma – 500 Torr Ethane.....	51
33. $\Omega$ vs $I_{pin}$ 500 Torr Ethane (500 Ghz).....	51
34. $I_{lase}$ vs. Log[Rb] – 500 Torr Ethane.....	52
35. $\Delta$ – 300 Torr Ethane.....	53
36. Grotrain Diagram – Laser Pumped Rb Fluorescence.....	57

## List of Tables

Table	Page
1. Rb Spectroscopic Data.....	6
2. Alkali Quantum Efficiencies.....	8
3. Model Variable Definitions (Rb DPAL).....	23
4. Baseline Parameters – Frequency Independent Case.....	33

## List of Symbols

Symbol	Definition
$A_{ji}$	Einstein A-coefficient
$c$	speed of light (in vacuum)
Cs	Cesium
$E$	ethane concentration
Fr	Francium
$g_i$	degeneracy of $i^{\text{th}}$ state
$g_{\text{th}}$	threshold gain
H	Hydrogen
$h$	Planck's Constant
He	Helium concentration
$I_{\text{pin}}$	Incident Pump Intensity
K	Potassium
$k_{32}$	spin-orbit mixing rate (ethane partner)
$k$	Boltzmann Constant
Li	Lithium
$l_g$	gain cell length
Na	Sodium
$N_i$	population density of $i^{\text{th}}$ level
$\eta$	quantum efficiency
$r$	net cavity reflectivity

Symbol	Definition
Rb.....	Rubidium
T .....	gain cell temperature
$t_{21}$ .....	radiative lifetime of upper laser level
$t_{31}$ .....	radiative lifetime of upper pump level
$\nu_{21}$ .....	frequency of the laser beam
$\nu_{31}$ .....	frequency of the pump beam
$\lambda$ .....	wavelength
$\pi$ .....	3.1415926
$\Delta E$ .....	energy differential
$\sigma_{21}$ .....	absorption cross section on the lasing transition
$\sigma_{31}$ .....	absorption cross section on the pump transition
$\Omega$ .....	longitudinally averaged two-way intracavity pump beam intensity
$\Psi$ .....	intracavity average two-way laser intensity
t .....	net cavity transmission
$\Delta\nu_{31}$ .....	pump beam bandwidth

# BROADBAND PUMPING EFFECTS ON THE DIODE PUMPED ALKALI LASER

## I. Introduction

### Background

For decades the United States Military has been researching and developing high energy lasers (HEL) for improved tactical advantages and anti-ballistic missile defense. These weapons offer numerous advantages over conventional systems, and as Secretary of the Air Force Widnall recognized in 1997: “It isn’t very often an innovation comes along that revolutionizes our operational concepts, tactics and strategies. You can probably name them on one hand – the atomic bomb, the satellite, the jet engine, stealth, and the microchip. It’s possible the airborne laser is in this league.” With pinpoint accuracy, HEL are capable of reducing collateral damage while achieving target destruction. Their light speed trajectory enables them to engage targets immediately after detection from a relatively safe distance. And finally, they are inexpensive to operate and can be tailored for other purposes, including non-lethal destruction, and disruption [8].

The currently mounted HEL on the Airborne Laser (ABL) has proven effective yet possesses a few undesirable characteristics. In February 2010, The ABL flew over the coast of California and successfully targeted, tracked, and destroyed a ballistic missile in its boost phase. This historical feat marks a breakthrough in operational status and revolutionizes warfare. In fact, the Missile Defense Agency officially recognized this

fact by awarding its Technology Pioneer Award to three Boeing Airborne Laser Testbed engineers and three of their government and industry teammates. Yet while this achievement is groundbreaking and a warfare game-changer, criticism over the installed systems logistical feasibility, size, and ammunitions reservoir is justified. This system is a chemically driven laser which utilizes vast quantities of hazardous chemicals including chlorine, iodine, hydrogen peroxide and potassium hydroxide, none of which are ideal for storage in a war zone. After exhausting its 6-10 shot magazine depth, it would take two C-17 transport planes to refuel, and due to atmospheric turbulence the ABL has a limited range of approximately 600 km for liquid fueled ICBM and 300 km for solid fueled ICBM. In addition, it takes the entire hull of a Boeing 747 to create weapons grade power. However, it is still the only system capable of such high power on target. With these factors in mind a pursuit for a lightweight, compact, low hazard risk, and high magazine depth system has been underway.

### **The Diode Pumped Alkali Laser**

According to experts in the field, the system which holds the most promise for achieving these standards is the Diode Pumped Alkali Laser (DPAL). It was first demonstrated in the early 90's and patented by Krupke in 2003 [5]. These systems utilize the cost and energy-effectiveness of diode bars, the thermal management advantages of gas phase lasers, the simplicity of alkali earth metals, and are essentially an efficient narrow-banding, laser photon engine [2].

An alkali, typically Rubidium (Rb) or Cesium (Cs), is heated to its gas phase and subject to diode-driven laser light in resonance with its second lowest excited state ( $^2P_{3/2}$ ). A spin-orbit relaxer induces a rapid Boltzmann Equilibrium between the upper pump

state to the upper lasing state, or the lowest lying excited state ( $^2P_{1/2}$ ). Spontaneous emission from the  $^2P_{1/2}$  state to ground induces amplified stimulated emission leading up to lasing. The energy level diagram below shows the optical-atomic and kinetic processes involved.

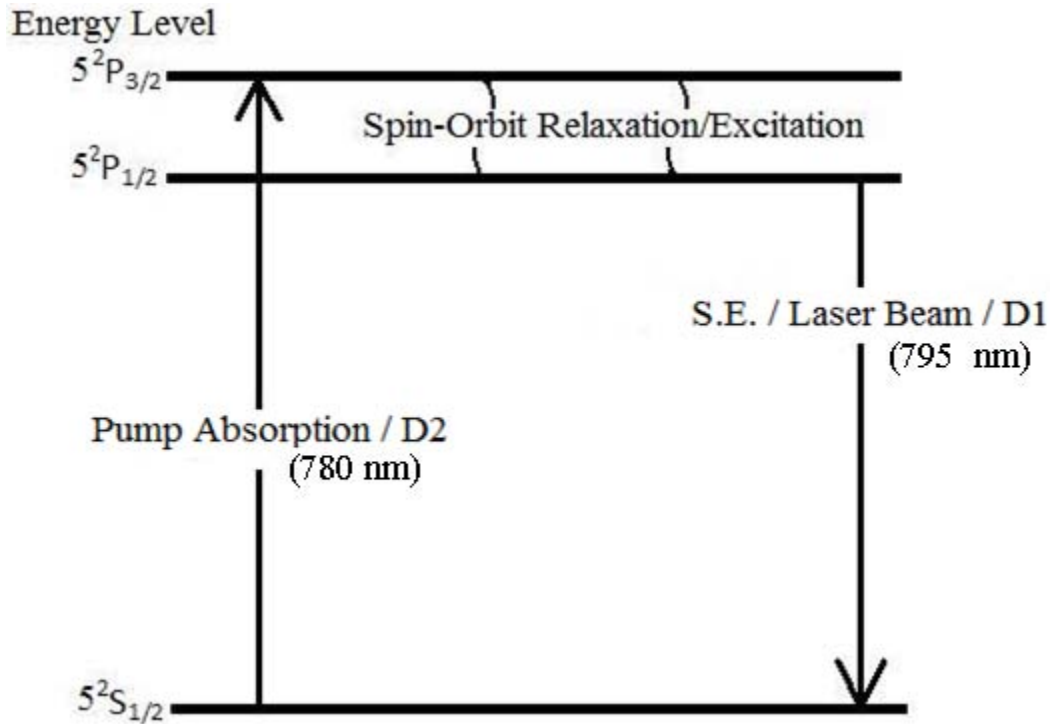


**Figure 1. DPAL Three Level Diagram (Rb)**

The DPAL mass produces single mode, narrow-banded, near infrared (IR) laser photons in a cyclic, three step process. As shown above, broadband, multimode diode laser light centered at the D<sub>2</sub> transition is incident on a vaporized alkali and buffer gas mixture. This light excites the alkali into its second excited state. With the proper buffer gas to alkali concentrations, rapid Boltzmann Equilibrium occurs through collision



processes causing relaxation from the upper  $^2P_{3/2}$ , to the lower  $^2P_{1/2}$  state [2]. While the energy split between the upper pump and upper lasing level is less than 1% of the pump energy, at projected operating temperatures this equilibrium still places over 45% of the alkali atoms in the upper lasing state, resulting in a high population inversion. Once the alkali is in this state, (the upper lasing level), it slowly (with a radiative lifetime of 27.7 ns [5]), yet eventually begins to fluoresce back to ground. This causes those slowly trickling spontaneous emission photons to see an inverted landscape upon release. Once ejected, they pass through the gain medium and by stimulated emission “grab” photons from other excited  $D_1$  atoms. As they grab these photons the projecting wave gains in amplitude through amplified spontaneous emission (ASE) until reaching the end of the gain cell.

Given a laser cavity and an emission trajectory within a mode of the respective cavity, and assuming our gain exceeds threshold, this amplified wave will oscillate back and forth through the gain medium exponentially increasing in amplitude after each pass. Eventually and after multiple passes, the stimulated emission rate caused by the high intensity oscillating laser beam overcomes the pump and spin-orbit relaxer rates, leading to a saturated  $D_1$  to ground transition and the maximum intra-cavity laser intensity [2].

### **Analytical Modeling**

In order to accurately model these events and predict the output beam strength of the DPAL, a robust and quasi-analytic model has been developed by Dr. Gordon Hager [2]. This model accounts for all the substantial interactions and effects associated with DPAL operation, including input beam intensity, alkali concentration, buffer gas concentration, mirror reflectivity, cavity transmittivity and gain medium length. It integrates

fundamental laser physics with experimental results specific to the DPAL to produce feasible and accurate results.

It has been advanced in order to take into effect the frequency dependence of the pump beams interaction with the system. It creates an alkali cross-section bandwidth function that is dependent on temperature and pressure, and also adds a frequency dependence to the pump beam intensity. It shows that a close spectral overlap between these two functions is paramount for optimal efficiency. Finally, it is also a beneficial tool for analysis of gain medium kinetics, parametric studies, and helps to improve the overall intuition of the staff, in hopes that a more clear and fundamental understanding will lead to an efficient, powerful, and precisely controlled system.

## II. Literature Review

In this chapter, a review of literature pertaining to the physics involved with the DPAL is summarized. Also summarized is a review of publications on advancing DPAL technology and a few small references to laser engineering. After establishing the theoretical foundations of the DPAL and its current state of affairs an introduction to the analytic model is made in the following chapter by a review of two of its author's publications.

### Alkali Earth Metals

Alkali earth metals (alkalis) have been extensively researched and are an ideal candidate for an optically pumped gain medium. First, they consist of the elements possessing a single valence electron, making their electron energy levels relatively easy to assign and well documented. The National Institute of Science and Technology has publicized a table consisting of the more significant spectroscopic constants for each element, and an excerpt from the table for Rb is shown below:

**Table 1. Rb Spectroscopic Data [5]**

Wavelength (nm)	$A_{ki} \text{ s}^{-1}$	Configurations	Terms	$J_i \ J_k$	$g_i \ g_k$
740.81731		$4p^6 5p - 4p^6 7s$	$2P^* - 2S$	$3/2 - 1/2$	$4 - 2$
761.8933		$4p^6 5p - 4p^6 5d$	$2P^* - 2D$	$1/2 - 3/2$	$2 - 4$
775.76507		$4p^6 5p - 4p^6 5d$	$2P^* - 2D$	$3/2 - 5/2$	$4 - 6$
775.94363		$4p^6 5p - 4p^6 5d$	$2P^* - 2D$	$3/2 - 3/2$	$4 - 4$
780.0268	$3.81 \times 10^7$	$4p^6 5s - 4p^6 5p$	$2S - 2P^*$	$1/2 - 3/2$	$2 - 4$
792.526		$4p^6 4d - 4p^6 8f$	$2D - 2F^*$	$5/2 - 7/2$	$6 - 8$
792.5537		$4p^6 4d - 4p^6 8f$	$2D - 2F^*$	$3/2 - 5/2$	$4 - 6$
794.7603	$3.61 \times 10^7$	$4p^6 5s - 4p^6 5p$	$2S - 2P^*$	$1/2 - 1/2$	$2 - 2$
827.141		$4p^6 4d - 4p^6 7f$	$2D - 2F^*$	$5/2 - 7/2$	$6 - 8$
827.1707		$4p^6 4d - 4p^6 7f$	$2D - 2F^*$	$3/2 - 5/2$	$4 - 6$
886.8512		$4p^6 4d - 4p^6 6f$	$2D - 2F^*$	$5/2 - 7/2$	$6 - 8$
886.8852		$4p^6 4d - 4p^6 6f$	$2D - 2F^*$	$3/2 - 5/2$	$4 - 6$

A tabulation of each electronic transition in Rb corresponding to photonic wavelengths from 740-880 nm along with the key spectroscopic constants of Einstein A coefficients (column 2), initial and final electronic configurations (column 3), and the degeneracy's of the initial and final states (column 5). Key transitions in the DPAL (D<sub>1</sub> at 795 nm and D<sub>2</sub> at 780 nm) have well known wavelengths, Einstein A-coefficients, degeneracy ratios, and spin states. For a more complete listing of data for Rb see Appendix A. The absorption cross-section is dependent on the Einstein A-coefficient and is given by:

$$\sigma(\lambda) = \frac{\pi^2 e^2}{m^2 c} \frac{g_2}{g_1} A_{21} \frac{1}{\lambda^2} L(\lambda) \quad (1)$$

Where  $g_2$  is the *degeneracy* of the upper transition state and  $g_1$  of the lower.  $A_{21}$  is the *Einstein A coefficient*,  $\lambda$  is the transition *wavelength*, and  $L(\lambda)$  is the normalized, unitless, *lineshape function* (typically a Gaussian, Lorentzian, or Voigt profile). It is apparent that absorption cross-sections scale linearly with Einstein A coefficients and it should also be noted that alkalis possess some of the largest coefficients currently known, at linecenter the D<sub>1</sub> transition absorption cross-section has a published value of  $4.92 \times 10^{-13} \text{ cm}^2$  [2,5]. Given such high cross-sections, alkalis are easily and efficiently energized through a radiant source, or in the case of the DPAL, through diode laser pumping.

Another characteristic amongst the alkalis that proves them an effective laser gain medium is their extremely high quantum efficiency (QE). In a laser, QE refers to the ratio between the excitation transition and the lasing transition. Mathematically stated:

$$QE = \frac{A_{21}}{A_{21} + A_{12}} \quad (2)$$

Where  $\eta$  is the QE,  $\Delta E_{\text{pump}}$  and  $\Delta E_{\text{laser}}$ , are the pump and laser transition energies respectively. It is the upper limit for the performance of any laser. It cannot be designed and is solely dependent on energy levels of the gain medium. However, lasers can be designed around QE, and the DPAL, having only a three step process and merely a fine structure split between its pump and upper lasing state, has remarkable QE. A tabulation of each alkali's QE is shown here:

**Table 2. Alkali Quantum Efficiencies [5]**

Alkali	$\Delta E_{\text{pump}}$ (eV)	$\Delta E_{\text{laser}}$ (eV)	QE	$\Delta \nu$ (GHz)
H	1.8887008	1.8886887	0.9999936	2.9257441
Li	1.84786	1.847818	0.9999773	10.155475
Na	2.10442907	2.10229704	0.9989869	515.51853
K	1.61711291	1.60995774	0.9955753	1730.0989
Rb	1.589049	1.5595909	0.9814618	7122.8813
Cs	1.45520606	1.38648645	0.9527767	16616.198
Fr	1.7263556	1.5172452	0.8788718	50562.275

Each alkali is listed with its photonic pump and laser energy, the QE, and the difference in frequency ( $\Delta \nu$ ) between the pump and laser transition. Such high QE are ideal for optimal performance but a large enough frequency gap must be maintained in order to avoid spectral overlap between the absorption and lasing transition. As will be shown, alkalis under current experimental conditions have absorption cross-sections with a full width half max (FWHM) on the order of 100s of MHz, leaving plenty of room (for most of the alkalis) in frequency space to avoid significant overlap. However, it is this authors opinion that Rb or Cesium (Cs) are the most ideal candidates. They maintain very high QE ( $> 95\%$ ), and have thousands of gigahertz in spacing between their

transitions, boosting confidence that, even at high pump intensities and alkali concentrations, any lineshape overlap is negligible.

While alkalis possess extremely high absorption cross-sections, and have remarkable QE, as mentioned before, matching the spectral bandwidth of the pump source to the  $D_2$  absorption profile is paramount for optimal efficiency [9]. In order to accurately model this profile any broadening or shifting of its hyperfine structure must be well accounted for. Figure 2 below diagrams the hyperfine structure on the  $D_2$  transition for Rb:

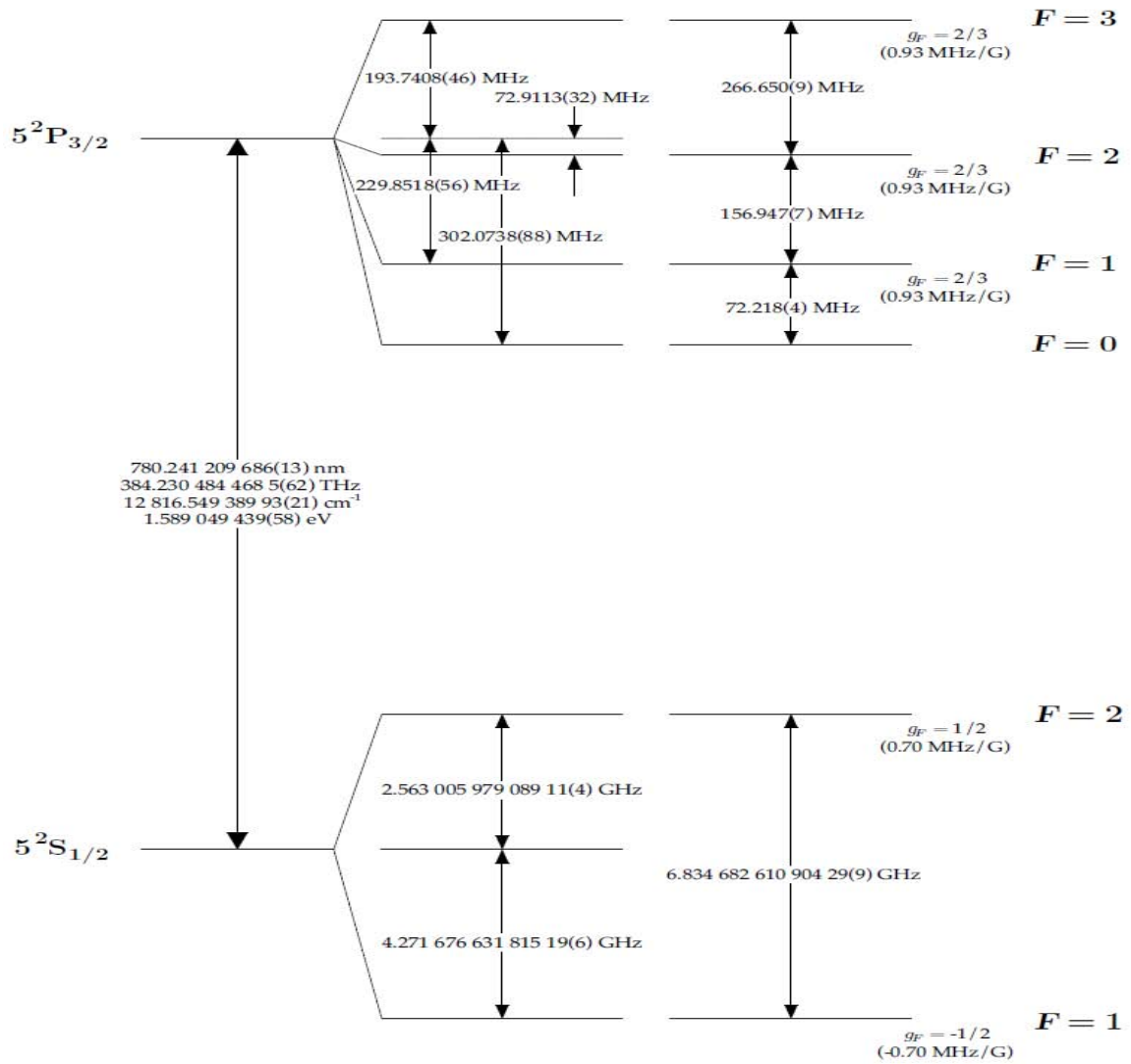


Figure 2. Rb  $D_2$  Hyperfine Structure [13]

As seen, there are four hyperfine components in the  $5^2P_{3/2}$  state and two components in the  $5^2S_{1/2}$ . However, the selection rules of  $\Delta F = 0, \pm 1$  allows for only a total of four transitions within the  $D_2$  line. Recently published data by Pitz *et al* has observed and accurately modeled the Doppler and pressure broadening rates as well as any pressure shifts associated with each of these transitions for Cs. It gives the net absorption cross-section as:

$$\text{---} \quad \text{---} \quad (3)$$

Where  $g_j$   $2J+1$  is *fine structure degeneracy*,

$\nu_{F' \rightarrow F''}$  is *linecenter frequency* of the  $F' \leftarrow F''$  hyperfine component,

$\lambda$  is  $c/\nu$ ,  $A_{21}$  is the *spontaneous emission rate*,

$S_{F'F''}$  is the *hyperfine line strength* for the  $F' \leftarrow F''$  component,

$G_V(\nu, \nu_{F' \leftarrow F''})$  is the *Voigt lineshape centered at  $\nu_{F' \leftarrow F''}$* ,

$f_{iso}$  is *relative natural abundance of Rb*, and

$f_{F''}$  is the *statistical distribution of population among  $F''$  states*.

This model has zero fit parameters and agrees with high precision experimental data. However, at high temperatures and pressures the cross-section blends into a single, pressure broadened line. These rates are determined for Cs, a very similar element to Rb. Therefore, the broadening rates determined by this fit are used to approximate a single Lorentzian for the  $D_2$  transition absorption cross-section. At sub-atmospheric pressures however, a peak cross section value error of 13% has been reported. This error decreases with pressure, and the DPAL will potentially operate above a single atm in order to maintain high spin-orbit relaxation. Such accuracy in the absorption lineshape will allow for a Gaussian diode beam to be narrow-banded for maximum absorption [9].

By narrow-banding the pump beam in such a way and maintaining proper buffer gas to alkali concentrations, and assuming no lasing, the initial pump rate and spin-orbit relaxation rate far exceed the spontaneous or stimulated emission rate on the lasing transition. This leads to a saturated D<sub>2</sub> transition and the upper two levels at their Boltzmann distribution. In this instance the kinetics of the system can be modeled by the following equations:

$$\frac{dN_1}{dt} = -\frac{N_1}{\tau_{sp}} + \frac{N_2}{\tau_{sp}} \quad (4)$$

$$(5)$$

$$(6)$$

Where  $N$  is the total alkali concentration,  $N_1$  are the *populations* in the ground, upper laser, and upper pump state respectively,  $g_1$  are the *degeneracies* associated with those states,  $\Delta E$  is the *energy split* between the upper two levels,  $k$  is the *Boltzmann Constant*, and  $T$  is *temperature*. In this instance two limits are being achieved simultaneously, the “bleached” pump transition limit, and the quasi two-level (Q2L) limit. The bleached limit corresponds to a fully saturated pump transition and the Q2L refers to the dynamics when the spin-orbit relaxation rate far exceeds the spontaneous or stimulated emissions rate on the lasing transition. Solving this system of equations gives the pre-lasing populations of the three states involved, and as mentioned before, at room temperature places over 45% of the population in the upper laser level, while leaving only 17% in the ground. Such a high inversion allows for gain above threshold to be achieved relatively easily. Figure 3 on the following page shows the inversion ratio between the  $^2P_{1/2}$  and ground level as a function of cell temperature:



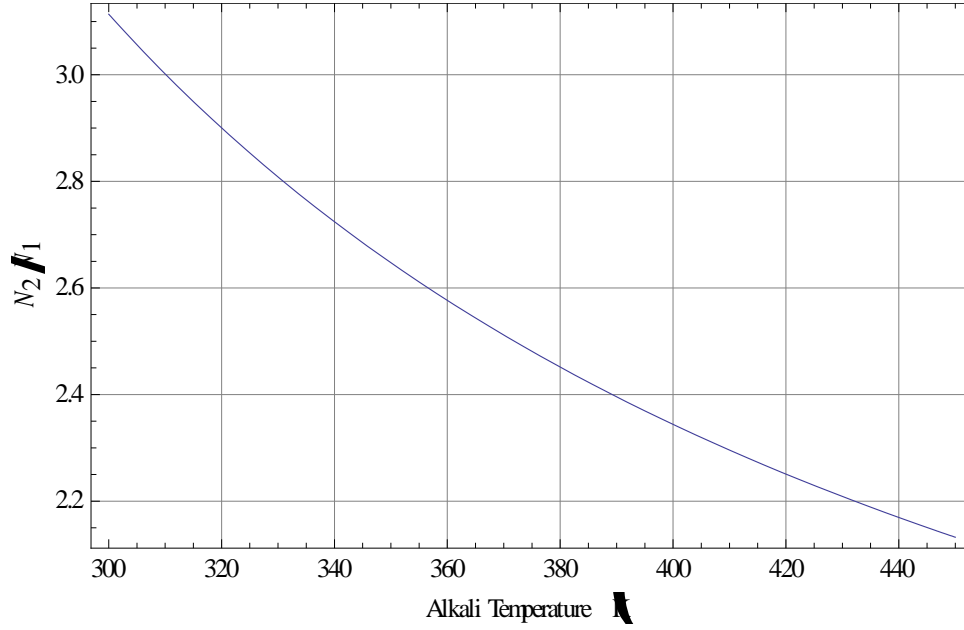


**Figure 3. Initial Population Inversion vs. Alkali Temperature**

As shown, alkalis (specifically Rb), are capable of high inversions through a combination of three factors: favorable degeneracy ratios between states, rapid interaction with buffer gases, and a significant Boltzmann differential.

In order to ensure this inversion is maintained and accurately predict gain medium kinetics precise knowledge of the dynamics between the alkali and buffer gas is requisite. This dynamic enters the laser rate equations in the form of the spin-orbit mixing rate coefficient,  $k_{32}$  with units of  $\text{cm}^3/\text{s}$ . The product of  $k_{32}$  and the buffer gas concentration ( $E$ ), in  $\text{cm}^{-3}$ , yields the number of collision induced energy transfers per atom per second. Its role is shown explicitly in equation 7, which is a portion of the lasing mode rate equation for the population density of the upper lasing state:

$$\frac{dN_2}{dt} = \dots \quad (7)$$

As shown, the spin-orbit mixing rate coefficient defines how quickly the upper two levels of the system equilibrate. The factor of two in equation 7 is due to the 2:1 degeneracy ratio between the hyperfine states of  $5^2P_{3/2}$  and  $5^2P_{1/2}$  in Rb, respectively. Theoretically the rate constant is defined as:

$$\frac{1}{\tau} = 2 \mu V_{\text{avg}} \sigma \quad (8)$$

Where  $V_{\text{avg}}$  is the *average relative velocity* of the collision pair,  $\mu$  is the *reduced mass* of the collision pair, ( $\mu = [(M_{\text{Rb}}M_{\text{Me}})/(M_{\text{Rb}}+M_{\text{Me}})]$ ), and  $\sigma$  is the *spin-orbit relaxation cross-section*. This rate has a published value of  $5.2 \times 10^{-10} \text{ cm}^3/\text{s}$ , and at 700 torr of buffer gas, cycles each atom through the lasing process many millions of times per second [16]. This allows for relatively low alkali concentrations to create high power intracavity beam intensities, potentially minimizing thermal management issues.

This spin-orbit kinetic process cannot be fully analyzed without an accurate account of the alkali concentration. At projected operating temperatures alkalis are in their liquid phase, and do not reach their boiling point until 1032 K. However, in liquid phase there is still a small percentage of atoms in their gas phase due to the slight probability of Rb atoms separating from the lattice by means of constructively interfering phonons, localized “hot spots” within the liquid, or any other thermally induced energy influx. A compilation of Rb data by Steck gives a rough guide to this percentage in terms of vapor pressure in Torr and is given by equation 9 below:

$$P_v = 10^{-10} \exp\left(\frac{10000}{T}\right) \quad (9)$$

where  $P_v$  is the *alkali vapor pressure* in Torr [13]. A graph of this pressure near projected operating temperatures is shown here:

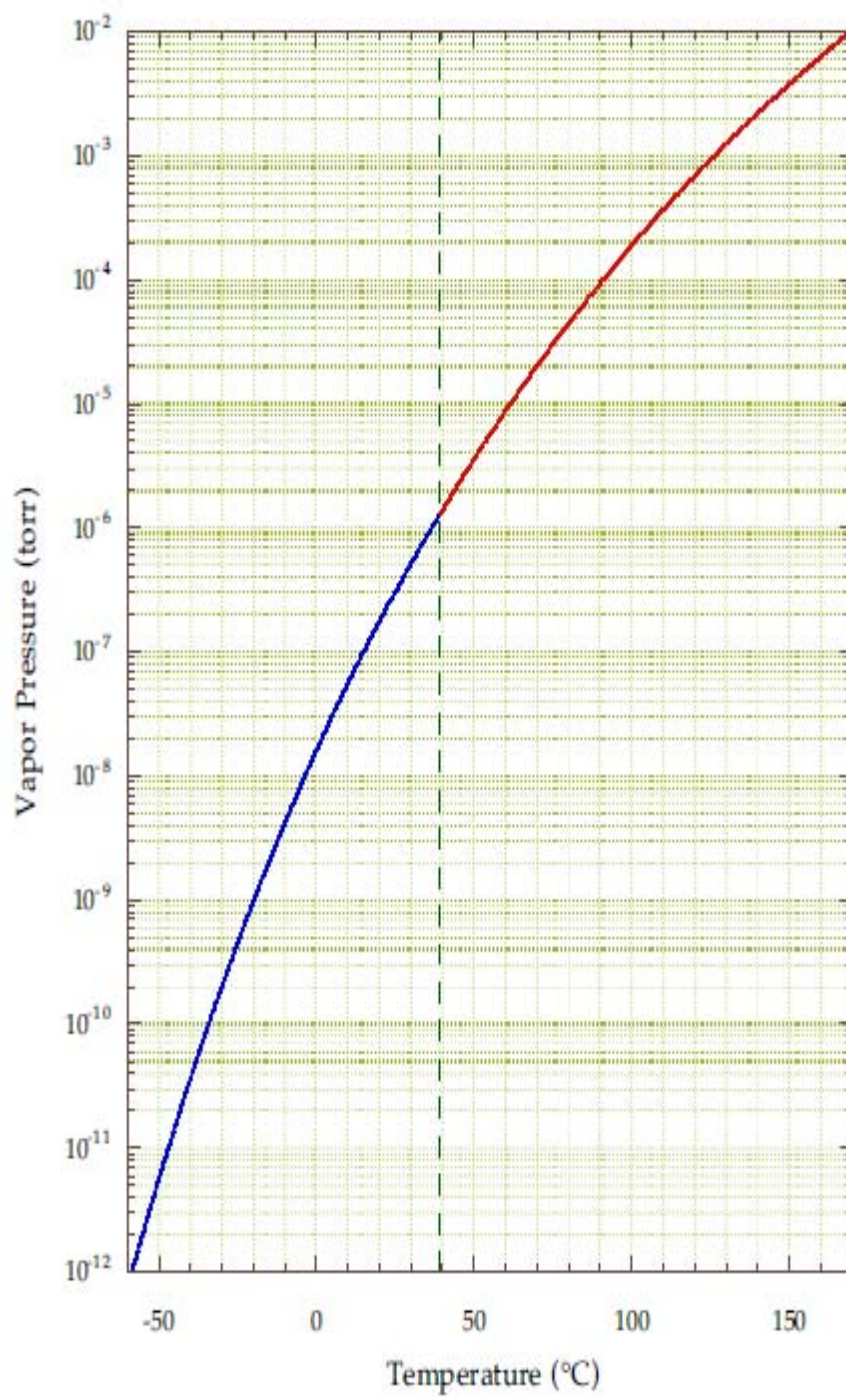
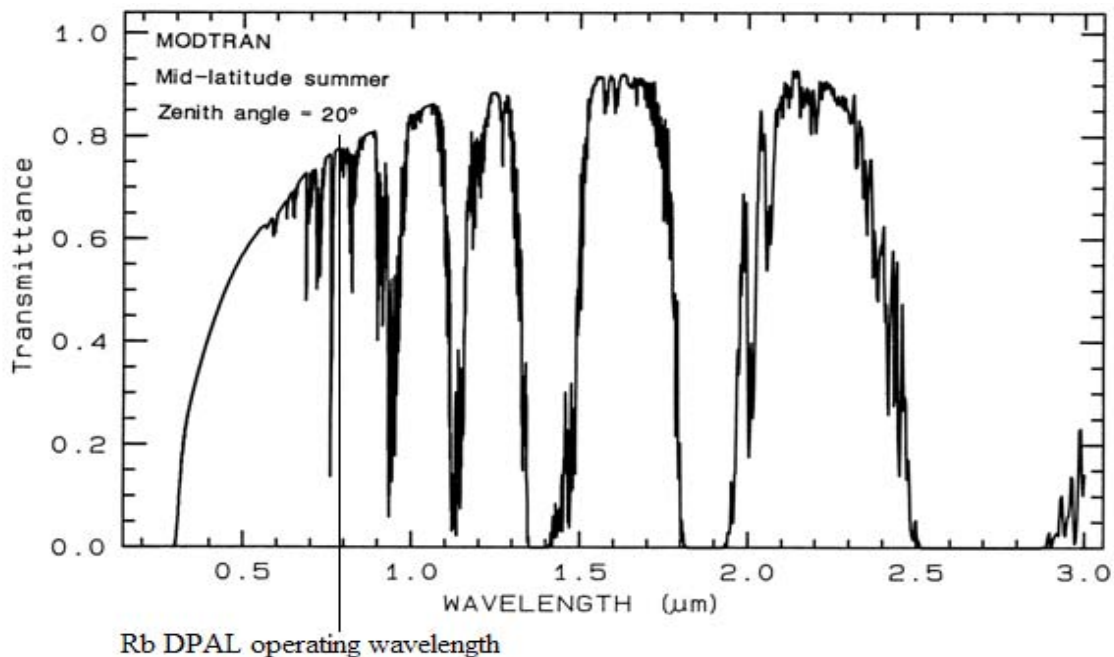


Figure 4. Rb Vapor Pressure vs. Temperature [13]

A final prerequisite for the feasibility of the DPAL to produce weapons grade intensity and beam quality on target is high atmospheric transmittivity. Atmospheric attenuation is devastating to the advantages of laser quality radiation, and can greatly reduce the effective range of the weapon. Absorption bands of the atmospheres constituent particles lead to diminishing intensity, dispersion, and diffraction causing a relatively weak and dispersed radiative strike. However, at the operating wavelength of the Rb based DPAL (795 nm), there is a transmission window with a transmittivity coefficient of over 80%. That figure is the value for the transmission through the entire atmosphere, holding promise that even higher transmission will occur for the projected operating range of the ABL (~500 km). Figure 5 shows the atmospheric percent transmission for a broad range of wavelengths given a Zenith angle of 20 degrees:



**Figure 5. Atmospheric Transmittivity**

Alkali earth metals have been chosen as the gain medium in the DPAL for a wide variety of reasons. First, there is a strong foundation of knowledge regarding their fundamental subatomic structure. Second, they possess remarkable QE, high absorption probabilities, and are capable of creating large population inversions. Also, each atom is capable of producing millions of laser photons per second through a high Boltzmann differential and accessible spin-orbit relaxation. They are easily vaporized at modest temperatures allowing for gas phase thermal management. They produce laser photons at frequencies within atmospheric windows, leading to high intensity weapons grade power on target. Finally, they are cheap, abundant and relatively easy to use, (albeit reactive to atmospheric exposure). They hold promise for high power, compact, efficient, and cost effective systems.

### **Diode Pumped Alkali Laser Technology**

The DPAL has generated much attention from many institutions including The Air Force Institute of Technology, Lawrence Livermore National Laboratory, University of New Mexico, Air Force Research Laboratory (AFRL) Directed Energy Directorate, Krupke Lasers and others. With so many entities in pursuit of realizing the potential of this system much progress has been made. It should be noted however that the DPAL technology is still in its early stages and there is still much design, engineering, experimentation and ingenuity required before this dream becomes a reality. Presented here is a review of publications pertaining to technological advancements of the DPAL.

Although gas phase lasers are inherently less effected by thermal heating, issues still arise and a gain medium flow system has been successfully designed, developed and demonstrated by AFRL. This system flows the alkali-buffer gas gain medium through

the resonator of the DPAL and carries away heat. By doing so, a fresh set of atoms is ready for the absorption-relaxation phases of the 3-step cycle and atoms lost to effects such as multi-photon absorption, collisional excitation into higher lying states, ionization or other processes outside the 3 level model are flown out of the cavity [11]. This is a significant first step towards achieving excellent beam quality at high laser powers.

A high efficiency Rb DPAL has been demonstrated with a linear optical slope efficiency of 69%. In this setup, a static alkali/ethane/helium lasing vapor mix is pumped with an approximately 1 MHz bandwidth diode laser achieving a maximum output power of 490 mW. This was achieved with 400/50 Torr of ethane/helium and a 20% reflective output coupler. It also achieved an optical-optical efficiency of 31.5% with a large threshold of ~677 mW. Linear scaling on the efficiency was maintained showing the spin-orbit relaxation rate was high enough to maintain a quasi two level system, resulting in a proportional increase to laser intensity as input beam intensity is increased [8].

A second demonstration of a DPAL device by Sulham *et al* focusing on operating high above threshold and achieved an output power of over 32 times threshold while maintaining a linear slope efficiency between 39% and 49%. This places only 3% of the efficiency loss due to threshold values. It also suggests that no second order kinetic or optical processes are involved in this experimental setup, and with an output intensity of over 20 kW/cm<sup>2</sup> demonstrates relatively high output powers [13]. However, the pump beam is pulsed with a 100 ns pulse width and may not accurately represent continuous wave operation, since thermal effects would not be readily apparent. It is possible that second order or nonlinear effects may not set in until a greater time span. Figure 6 at the

top of the page 18 shows the basic setup for the static cell DPAL experiments mentioned above.

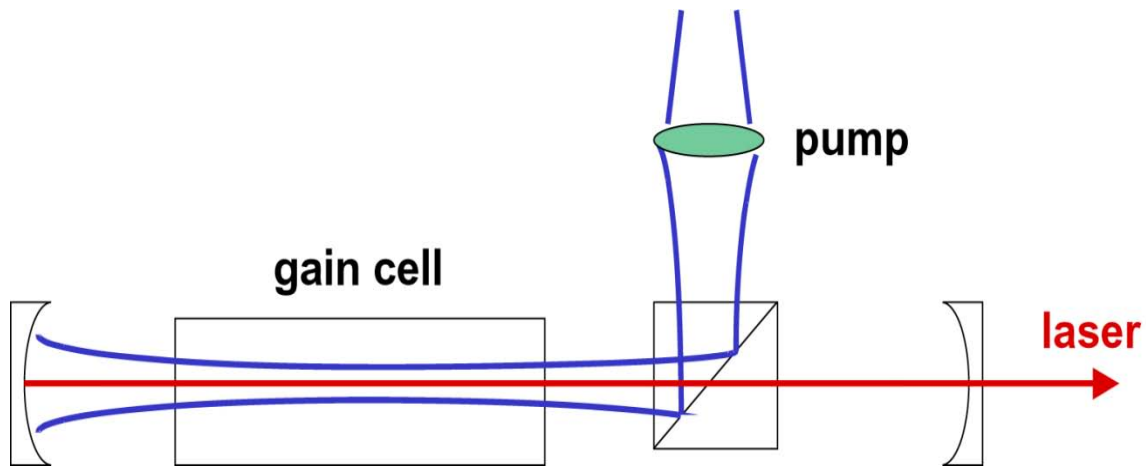


**Figure 6. Standard DPAL configuration**

An alternative approach to thermal management has recently been proposed by Zweiback *et al* that utilizes a high aspect ratio, liquid cooled copper waveguide which serves to both guide the pump beam and more quickly dissipate heat. In traditional DPAL designs, the volume of the gain cell far exceeds the actual gain volume and heat removal is only accomplished through conduction with the cells walls. The large spacing between the active region and the cell wall causes low thermal conductivity resulting in a thermally constricted upper limit on laser power. In this design, a copper core runs through the gain volume dissipating heat. It is also capable of heating depending on the state of lasing. Figure 7 at the top of the follow page shows the lasing head and gives output power as a function of time [17]:

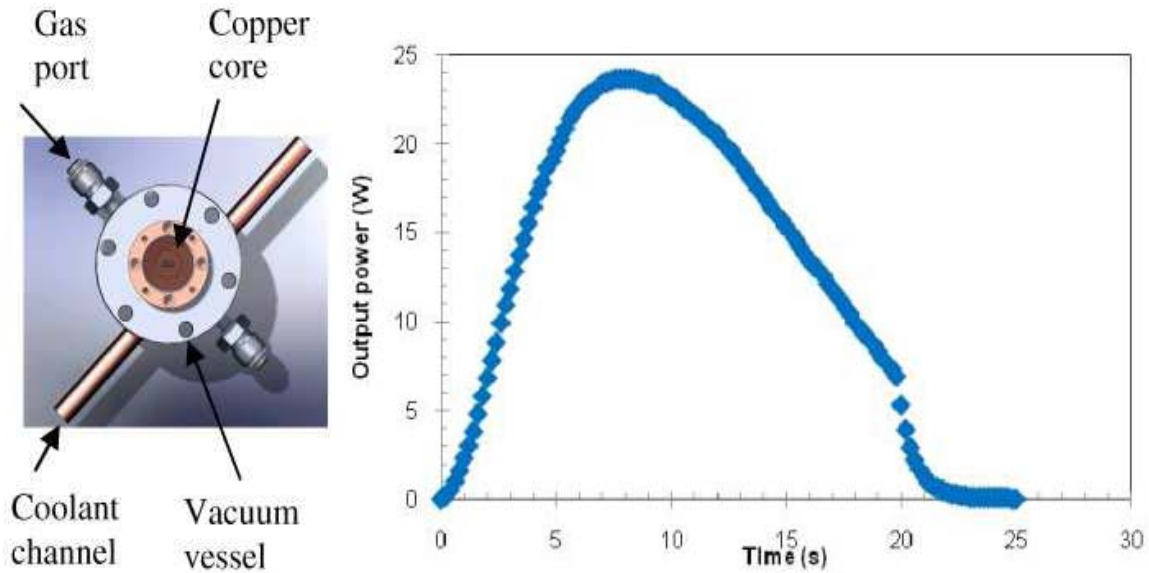


**Figure 7. Copper Waveguide Model and Results [17]**

As seen on the left, an offset coolant channel penetrates the gain medium rapidly dissipating or adding heat to the gain medium. The plot to the right, as interpreted by its author, is best described by thermally induced fluctuations in Rb concentration. Initially, Rb concentrations are below optimal, however through heating the vapor pressure is increased until the most effective concentration for the input beam strength is reached. Rollover begins as alkali concentration becomes high and the gain medium optically thick. Eventually lasing ceases after the pump beam is unable to penetrate the length of the gain cell and gain recedes below threshold. This design shows greater control over thermal management and may also be capable of being expanded to a time varying temperature control system that is based on the current output efficiency [17].

Since their advent in 2003, the DPAL has seen noteworthy improvement in its realization. Early DPAL demonstrations achieved maximum output powers of 1 to 3 Watts. Currently operating CW DPALs are in the 100's of Watts and the pulsed variety



in the 10's of kilowatts. Multiple initiatives into solving the thermal management issues associated with the DPAL have shown success. And third, impressive slope efficiencies have been observed in a variety of experiments. Research and design is ongoing and as more data is collected and rates and quantities defined they can be integrated into the model making it more precise and robust.

### **III. Methodology**

#### **Introduction**

Presented here is a derivation from fundamental laser physics of the analytic model developed initially by Dr. Gordon Hager and extended through the work of this thesis. The model is implemented in “Mathematica”, a leading computation software package in scientific academia. The initial derivation will neglect pump beam linewidth and derive solutions which are based on a single frequency delta function input beam. Afterwards, it will be shown that a frequency dependent pump beam intensity function is easily applied to the solutions of this more simple case. The model incorporates all of the currently published values for the various spectroscopic constants and broadening rates.

While this model is analytic in nature, it does rely on numerical integration of certain functions, and some approximations are made. However, these functions are continuous over the bounds of integration and have slopes much lower than the numerical integration step size, giving confidence in resultant values. Also, the model only analyzes a Rb based DPAL with an ethane/helium buffer gas mix. Approximations in regards to certain effects being neglected or deemed insubstantial will be addressed as they arise.

As mentioned in the abstract, the model produces an output beam intensity function dependent on seven input values. These include the input beam intensity, input beam linewidth, the Rb concentration, ethane concentration, mirror reflectivity, cavity transmittivity, and gain cell length. After incorporating all the fundamental aspects of the physics involved, plots are generated through “Mathematica” of the various effects changes in system parameters have on output beam intensity. The figure on the following page highlights all the essential features included in the model.

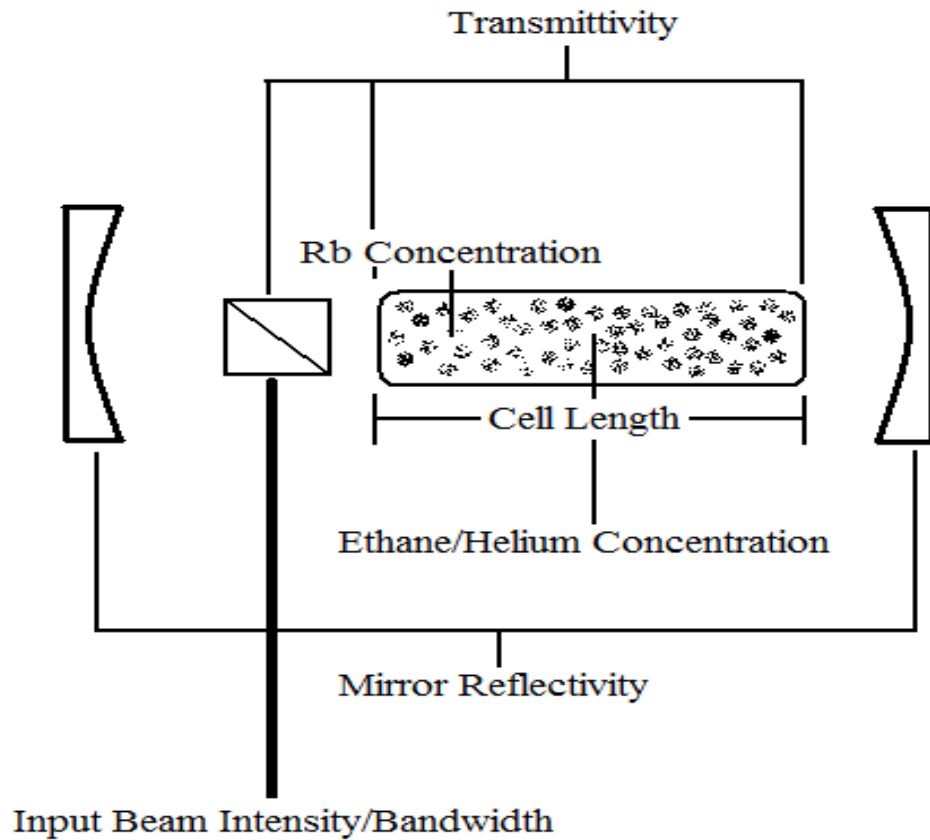


**Figure 8. Model Dependent Variables**

Shown in the standard layout above, the model has yet to incorporate spatial dynamics and is independent of cavity design. It is currently only capable of predicting output intensities, not net output power, cavity mode, or output beam quality. Being so, design engineers planning a system based on the results of the model will have freedom in design, constraining themselves only to meeting the parametric settings of the desired predicted output intensity. The pump linewidth extension has yet to be made on the lasing transition and its cross-sectional value is taken at its linecenter peak value. The table on the following page is to be used as reference throughout the derivation of the model and lists all symbols used with their definition and value (if applicable).

**Table 3. Model Variable Definitions (Rb DPAL)**

Symbol	Definition	Value	Units
$N_1$	concentration of atoms in ground state	variable	$\text{cm}^{-3}$
$N_2$	concentration of atoms in the $5^2P_{1/2}$ state	variable	$\text{cm}^{-3}$
$N_3$	concentration of atoms in the $5^2P_{3/2}$ state	variable	$\text{cm}^{-3}$
$N_{tot}$	alkali concentration	variable	$\text{cm}^{-3}$
$\sigma_{21}$	absorption cross section on the lasing transition	$*4.80 \times 10^{-13}$ (linecenter)	$\text{cm}^2$
$\sigma_{31}$	absorption cross section on the pump transition	$*4.92 \times 10^{-13}$ (linecenter)	$\text{cm}^2$
$\Omega$	longitudinally averaged two-way intracavity pump beam intensity	variable	$\text{W}/\text{cm}^2$
$h$	Planck's Constant	$6.626 \times 10^{-34}$	J-s
$\nu_{21}$	frequency of the laser beam	$3.774 \times 10^{14}$	Hz
$\nu_{31}$	frequency of the pump beam	$3.846 \times 10^{14}$	Hz
$k_{32}$	spin-orbit mixing rate (Ethane partner)	$5.2 \times 10^{-10}$	$\text{cm}^3/\text{s}$
$t_{21}$	radiative lifetime of upper laser level	27.7	ns
$t_{31}$	radiative lifetime of upper pump level	26.23	ns
$\psi$	intracavity average two-way laser intensity	variable	$\text{W}/\text{cm}^2$
$E$	Ethane concentration	variable	$\text{cm}^{-3}$
$l_g$	gain cell length	variable	cm
$R$	net cavity reflectivity	variable	N/A
$T$	net cavity transmission	variable	N/A
$K$	Boltzmann constant	$1.38065 \times 10^{-23}$	J/K
$T$	Gain cell temperature	variable	K
$g_{th}$	threshold gain	variable	$\text{cm}^{-1}$
$I_{pin}$	input beam intensity	variable	$\text{W}/\text{cm}^2$
$C$	speed of light (in vacuum)	$3.0 \times 10^8$	m/s
$\lambda_{31}$	pump wavelength	780.026	nm
$\lambda_{21}$	laser wavelength	794.76	nm
$\Delta\nu_{31}$	pump beam bandwidth	variable	Hz
$He$	Helium concentration	variable	$\text{cm}^{-3}$
$g_1$	degeneracy of ground state	2	N/A
$g_2$	degeneracy of upper laser level	2	N/A
$g_3$	degeneracy of upper pump level	4	N/A

## Longitudinally Averaged Two-Way Intracavity Pump Beam Intensity

We begin by defining the intracavity pump beam intensity. Consider the interaction between the pump beam at each transition through, or reflection off of, a component of the cavity. The intensity off the initial interaction with the beam splitter defines  $I_{pin}$ , from there the beam is incident on the first wall of the gain cell, receiving a transmission loss defined by  $t_p$ , resulting in an initial inner cell intensity of  $t_p I_{pin}$ . As the beam progresses through the gain cell, it receives a Beer's Law exponential gain given by:

(10)

where  $g_{31}$  is the *gain* on the pump transition. After exiting the cell another transmission loss is taken as well as a reflectivity loss defined as  $r_p$ . Finally, before re-entering the cell it experiences another transmission loss as it passes through the cell wall. This gives the intensities of the two initial input beams incoming from both ends of the cell as:

(11)

(12)

where  $I^+$  is the initial incident pump beam intensity and  $I^-$  is the intensity of the input beam after a single pass a reflection back into the gain medium. Figure 9 below shows the input beam intensity at each transition for a single round trip pass [2].

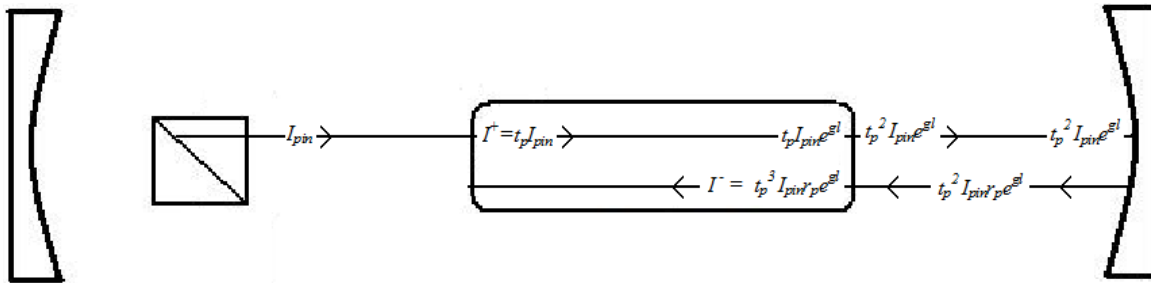


Figure 9. Round Trip Pump Beam Intensity

Assuming the beam is highly attenuated after a single round trip, the longitudinally averaged intracavity pump beam intensity can be defined by integrating the sum of these two incident beams across the length of the gain medium, and averaging the result. The explicit derivation is shown here:

$$\frac{1}{L} \int_0^L \left( I^+ + I^- \right) dz \quad (13a)$$

$$\frac{1}{L} \int_0^L \left( I^+ + I^- \right) dz \quad (13b)$$

$$\frac{1}{L} \int_0^L \left( I^+ + I^- \right) dz \quad (13c)$$

Substituting values from equations 11 and 12 for  $I^+$  and  $I^-$  yields:

$$\frac{1}{L} \int_0^L \left( I^+ + I^- \right) dz \quad (13d)$$

Ignoring transmission losses and assuming 100% pump beam reflectivity simplifies this equation to:

$$\frac{1}{L} \int_0^L \left( I^+ + I^- \right) dz \quad (13e)$$

Considering the beam is highly attenuated after its first pass and the first transmission loss could be incorporated into the initial beam intensity, the approximation in eqn. 13e will be used to define  $\Omega$ . In the same manner output laser intensity can be defined in terms of the average intracavity lasing intensity by [2]:

$$\Omega = \frac{1}{L} \int_0^L I^+ dz \quad (14)$$

## Laser Rate Equations

The dependence of both the intracavity pump beam and output laser intensity functions on alkali population densities demand solutions to the dynamic laser rate equations for evaluation. Assuming no second order, non-linear, or extraneous effects in the gain medium, the conservation of mass and the rate equations for the three states in the DPAL during steady state operation are defined as follows:

$$\text{---} \quad \quad \quad \text{---} \quad \quad \quad \text{---} \quad \text{---} \quad \text{---} \quad (15)$$

[illegible]

$$\text{---} \quad \text{---} \quad \text{---} \quad \text{---} \quad (17)$$

(18)

The first term in each rate equation, and the second term in eqn. 15 are the stimulated emission and absorption rate between either the pump, lasing beam or both. The second term in eqns. 16 and 17 are the dynamics of the spin-orbit Boltzmann equilibration, Finally, the remaining terms are the spontaneous emissions.

Solutions to these equations aren't readily available due to their non-linearity, however, eliminating eqn. 17 still gives an algebraic set which is easily solved through Mathematica. There are two sets of solutions, one for the non-lasing mode and one for lasing mode. In the non-lasing mode instance,  $\Psi = 0$  and for saturating pump intensities the population densities are defined by their values described in the literature review. In lasing mode,  $\Psi \neq 0$  and since the gain is clamped at threshold eqn 19 at the top of the following page can be used to solve for the populations and intracavity lasing intensity simultaneously [2].

$$\frac{1}{\Omega} \frac{d\Omega}{dt} = \frac{1}{\Omega} \left( \frac{d\Omega}{dt} \right) \quad (19)$$

The simultaneous solutions to the the steady state laser mode population densities and intracavity laser beam intensity are given by:

$$\frac{1}{\Omega} \frac{d\Omega}{dt} = \frac{1}{\Omega} \left( \frac{d\Omega}{dt} \right) \quad (20)$$

$$\frac{1}{\Omega} \frac{d\Omega}{dt} = \frac{1}{\Omega} \left( \frac{d\Omega}{dt} \right) \quad (21)$$

$$\frac{1}{\Omega} \frac{d\Omega}{dt} = \frac{1}{\Omega} \left( \frac{d\Omega}{dt} \right) \quad (22)$$

$$\frac{1}{\Omega} \frac{d\Omega}{dt} = \frac{1}{\Omega} \left( \frac{d\Omega}{dt} \right) \quad (23)$$

$$\frac{1}{\Omega} \frac{d\Omega}{dt} = \frac{1}{\Omega} \left( \frac{d\Omega}{dt} \right)$$

### Transcendental Solution

We now have solutions to the independent variables (population densities) for the intracavity pump beam, intracavity lasing beam, and output laser intensity. However, these variables are themselves dependent on the averaged intracavity pump beam intensity. This causes the solution for  $\Omega$  to be transcendental in nature, as in it is inherently a function of itself. Rewriting equation 13e to show this dependence explicitly:

$$\frac{1}{\Omega} \frac{d\Omega}{dt} = \frac{1}{\Omega} \left( \frac{d\Omega}{dt} \right) \quad (24)$$



As seen, in order to evaluate and obtain values for the intracavity pump intensity an input value for said intensity must be determined. It is only when both the independent variable value for  $\Omega$  and the function output value itself are equal is there a solution. These are found by solving the planar intersection between  $f(\Omega) = \Omega$  and  $\Omega$ . The graph below is an example of this intersection for typical DPAL parametric settings.

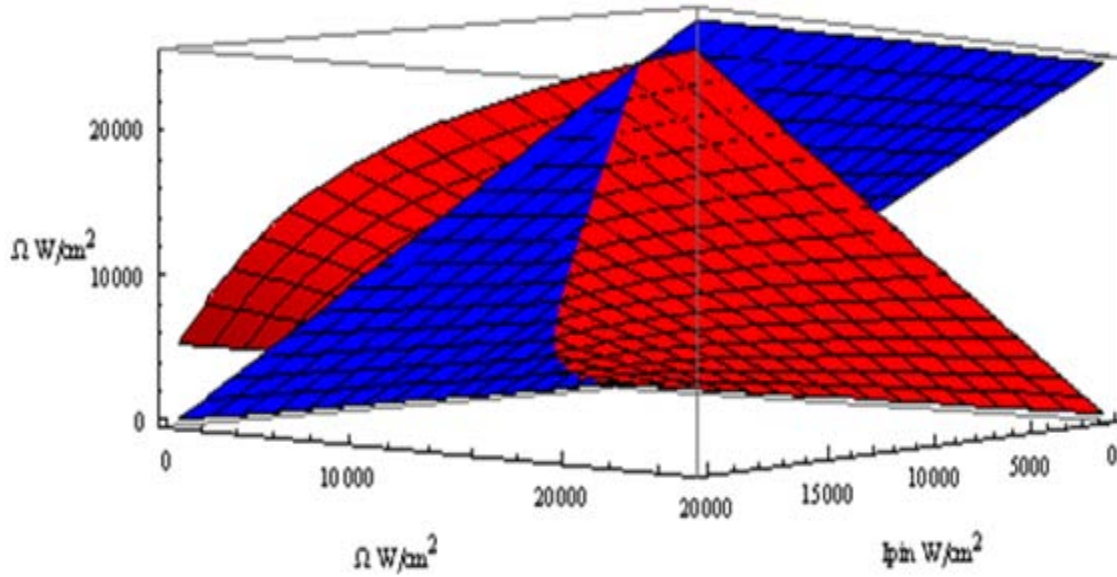


**Figure 10. Transcendental Intersection**

The intersection of the two functions shown above are the solutions, given the baseline parametric settings, to the intracavity longitudinally average pump beam intensity for  $I_{pin}$  values ranging from 0 – 20000 W/cm<sup>2</sup>. The model solves this intersection problem by solving for  $\Omega$  in the root equation below:

$$\frac{I_{pin}}{I_{th}} = \frac{1}{1 + \frac{I_{pin}}{I_{th}}} \quad (25)$$

In doing so explicit values which can be used as input into the intracavity laser intensity equation can be found and the model is capable of predicting output laser beam intensities based on the seven fundamental parameters within the system. Figure 11 below gives  $\Omega$  values for a range of input beam intensities with the baseline parametric settings found in table 4.

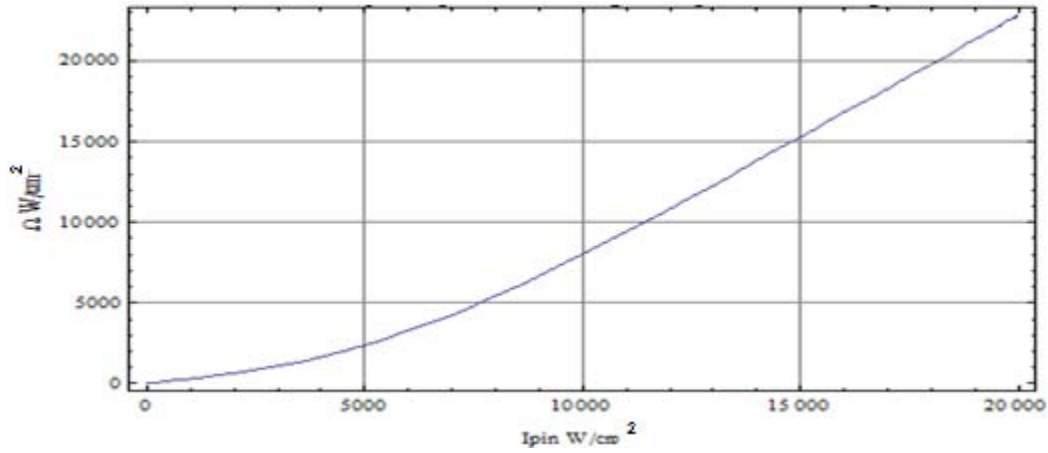


Figure 11.  $\Omega$  vs  $I_{pin}$

Given these solutions we rewrite the output beam intensity as an explicit function of input beam intensity, and thereby completing the frequency independent part of the model. With this ability, we now have a “black box” capable of taking in a set of parametric settings and giving us our desired result, output beam intensity, explicitly:

(26)

## Frequency Dependence of the Pump Transition

As mentioned, matching the pump beam spectral profile to the absorption cross-section lineshape is paramount for optimal efficiency. In order to model this, we must assign a frequency dependence to the absorption cross-section ( $\sigma_{31}$ ) and the input beam intensity ( $I_{pin}$ ). This is done by appending normalized frequency distribution functions onto the mentioned existing values:

(27)

(28)

Where  $f_{pump}$  is a normalized Gaussian Distribution and  $f_{31}$  is a pressured broadened Lorentzian Distribution. They are defined explicitly in equations 29 and 30.

$$\frac{f_{pump}}{f_{pump}} \quad (29)$$

$$\frac{f_{31}}{f_{31}} \quad (30)$$

For baseline operating conditions of 600 Torr of Ethane and Rb vapor concentrations corresponding to 393.15 K the pressure broadened width of the absorption cross section has a FWHM value of 19.73 GHz. By setting the diode FWHM to this optimistically narrow bandwidth excellent spectral overlap is achieved as shown in figure 12 below:

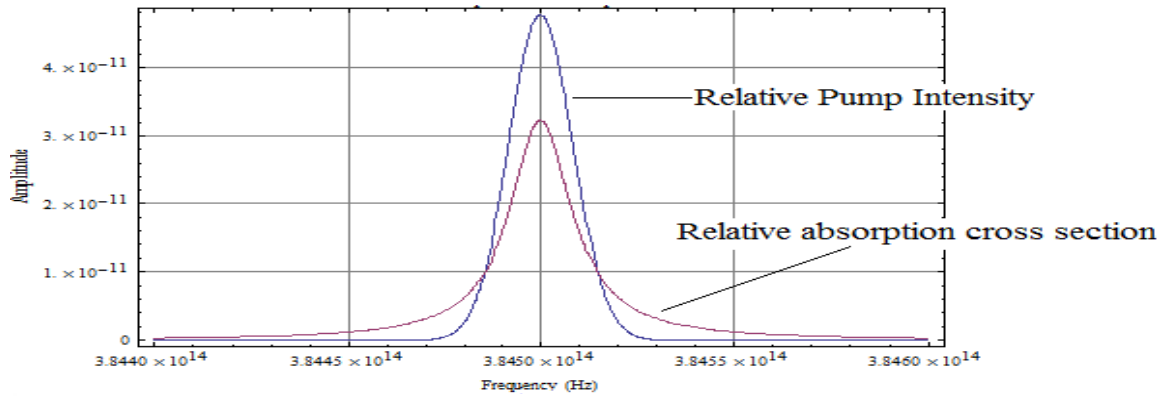


Figure 12. D1 Spectral Overlap [3]

The majority of the produced results set the FWHM of the absorption cross section to a predetermined value not coupled to cell temperature or buffer gas concentration. However a few plots incorporate the broadening effects associated with increased pressure and cell temperature, for those the FWHM is defined as:

$$\Delta \nu = \Delta \nu_0 \left( 1 + \frac{T}{T_0} \right)^{\frac{1}{2}} \left( 1 + \frac{E}{T} \right)^{\frac{1}{2}} \quad (31)$$

Where  $\Delta \nu_0$  is the published *broadening rate*,  $T_0$  is the *temperature* at which the rate was measured,  $E$  is the *ethane concentration* (or corresponding gas) and  $T$  is the current DPAL *operating temperature*.

Due to the frequency dependence of the input beam and absorption cross-section, the first term in equation 15 becomes an integral over frequency and algebraic solutions to the rate equations cease. However, a solution to the problem has been arrived through redefining the rate equations with an overall pump beam interaction term  $\Omega_f$ . It begins by adding a frequency dependence to the single frequency solution of  $\Omega$ :

$$\frac{dN}{dt} = -\frac{N}{\tau} + \Omega_f \quad (32)$$

Multiplying by the denominator (except for  $l_g$ ) and integrating over frequency gives:

$$\frac{dN}{dt} = -\frac{N}{\tau} + \Omega_f \quad (33)$$

The term on the left of eqn. 33 is the frequency dependent absorption and stimulated emission rate for the lasing transition, and is the term limiting an algebraic solution. By defining  $\Omega_f$  as this and substituting it into the rate equations solutions are once again

obtained for the population densities, however this time they are dependent on  $\Omega_f$ . This once again leads to a transcendental equation for  $\Omega_f$ , explicitly:

$$- \quad - \quad (34)$$

Solutions are again obtained through the root equation method, and new population density functions are generated independent of  $\Omega_f$ , and are now functions of  $I_{pin}$ . By doing so the “black box” is once again established and the frequency addition to the pump interactions has been accomplished. The output laser intensity is now a function of pump beam bandwidth as shown in eqn. 35.

$$(35)$$

With the ability to predict output laser intensity with 8 dimensions of variability in a quasi-analytic fashion the DPAL three level model is an excellent tool for analysis of projected future technologic endeavors. The few approximations that have been made are minimized or have been deemed insubstantial. For a complete layout of the code, with a brief Mathematica tutorial, see appendix b.

## IV. Results and Analysis

### Introduction

The code generates 2D and 3D plots describing laser performance characteristics including efficiency, pump beam output intensity, population density ratios, direct comparisons to single and multi-frequency cases, and others. The single frequency results are presented first and will be used for comparison with the broadband pump beam results. Each plot is accompanied with an analysis of the results given the implications that the graphs trends have on laser characterization. The 3D plots are capable of showing the simultaneous effect changes in multiple systems parameters have on the laser output making it easier to assign significance to each input variable.

The graphs generated are based on a set of “baseline” parametric settings. These correspond to recent experimental operating conditions and the values for the frequency independent segment of the code are given in the table below. The Rb concentration corresponds to a cell temperature of 393.15 K, the ethane concentration corresponds to a partial pressure of 300 Torr.

**Table 4. Baseline Parameters - Frequency Independent Case**

Variable	Value	Units
$l_g$	2	cm
$N_{tot}$	$1.85 \times 10^{13}$	$\text{cm}^{-3}$
E	$9.66 \times 10^{18}$	$\text{cm}^{-3}$
r	0.2	N/A
t	0.975	N/A

### Single Frequency, No Lasing Results

Consider the pre-lasing conditions of the DPAL under the frequency independent model. The steady state population densities as a function of  $\Omega$  are plotted in figure 13:

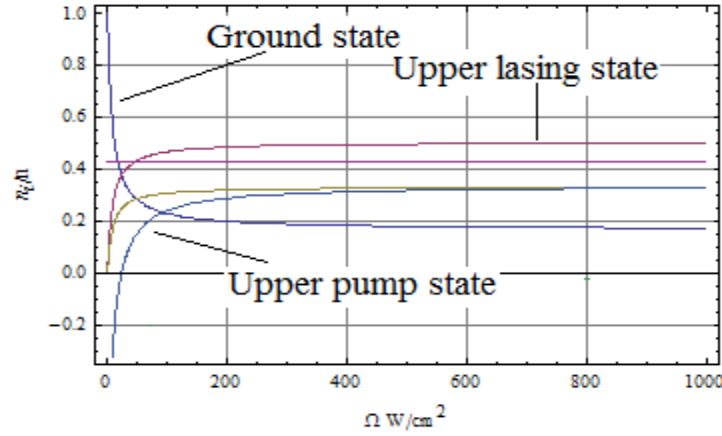


**Figure 13. Steady State Alkali Concentrations – Pre lasing**

As seen, as intracavity pump intensity increases each state asymptotically approaches their values described above in the literature review.

Figure 14 shows the intracavity intensity as a function of input beam strength. Initially the pump strength is not sufficient to fully penetrate the gain medium and becomes fully absorbed before a single pass through the cell. This can be seen in the low input beam powers of the graph where the slope efficiency is small. However, at approximately  $225 \text{ W/cm}^2$ , the beam is able to fully pass through the cell and a portion of the reflected wave contributes to  $\Omega$ . Eventually the gain medium becomes bleached and the two way intracavity beam intensity reaches its maximum slope efficiency of 2.

(36)

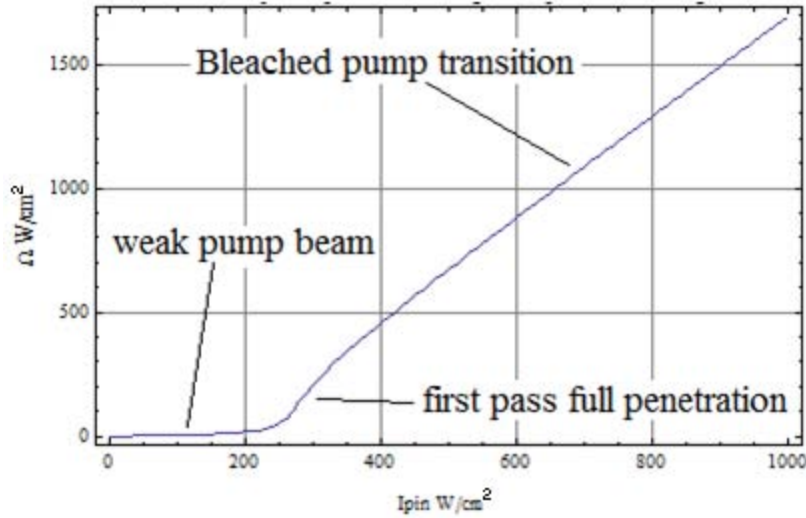


**Figure 14. Pre-Lasing Intracavity Pump Beam Intensity – Frequency Independent**

### **Single Frequency, Lasing Mode Results**

Presented in this section are the results for the frequency independent, steady state lasing mode case. The baseline parameters are the same from the previous section, and it is shown that these results coincide well the the pre-lasing mode results. Analysis of the frequency independent case will build intuition on the dynamics and interactions of the system paving the way for a clearer view of the effect that broadening the pump beam has on the DPAL. Recall in this instance the interaction between the pump beam and the system is represented with a delta function in frequency input intensity centered on the peak absorption cross-section value. Being so, we assume this represents the upper limit on absorption and for certain settings efficiency, output beam strength, and inversion ratios for a given input beam intensity. Figure 15 on the following page shows the oscillating intracavity laser intensity as a function of the intracavity beam intensity.



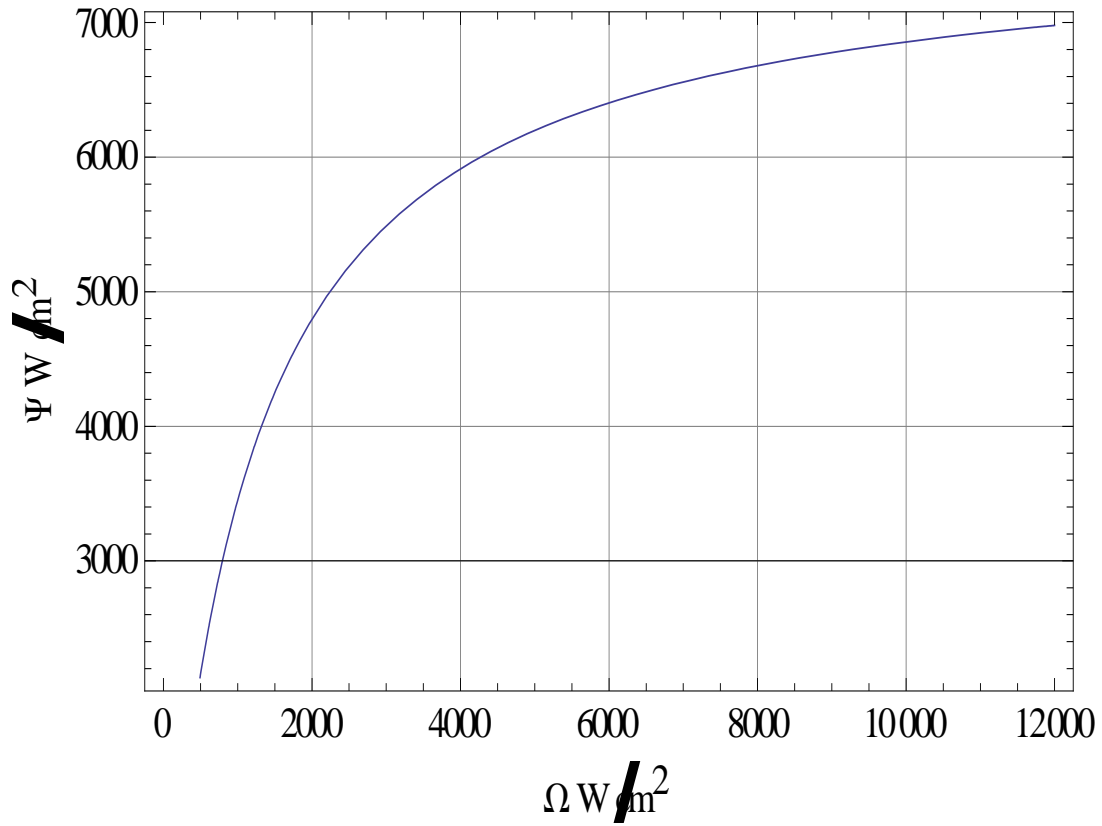


**Figure 15. Intracavity Laser Intensity – Frequency Independent**

Initially the pump beam is unable to reach threshold and  $\Psi$  is undefined. However, at an  $\Omega$  value of 40.04 W/cm<sup>2</sup> threshold is reached and lasing begins. The linear slope regime above represents the Q2L behavior with the spin-orbit relaxation able to keep up with the pump and laser transitions. Rollover occurs as these radiative transfer rates dominate the dynamics and the buffer gas is unable to equilibrate the alkali in time for the relatively high oscillating  $\Psi$  value to see an inversion. An asymptotic limit representing a bleached laser transition begins to develop at higher  $\Omega$  values. This threshold value corresponds well with the calculated threshold value of 40.3 W/cm<sup>2</sup> for the no lasing case, showing the model is well coordinated and precise.

The plot of the intracavity pump beam intensity as a function of input beam strength for the lasing case is similar to the non lasing except the curvature is described by different phenomena. As seen below, once again  $\Omega$  is slow to initially rise, then turns and hits a maximum slope efficiency. Initially the spin-orbit rate is able of cycling the atoms into the upper lasing state where the inversion with ground maintains amplification of the oscillating laser intensity. However, for the defined parametric settings, absorption begins to cease as the spin-orbit rate is unable to funnel atoms into the lower fine-structure level. This results in a linear slope efficiency of over 100%. This plot is shown in Figure 16 below:

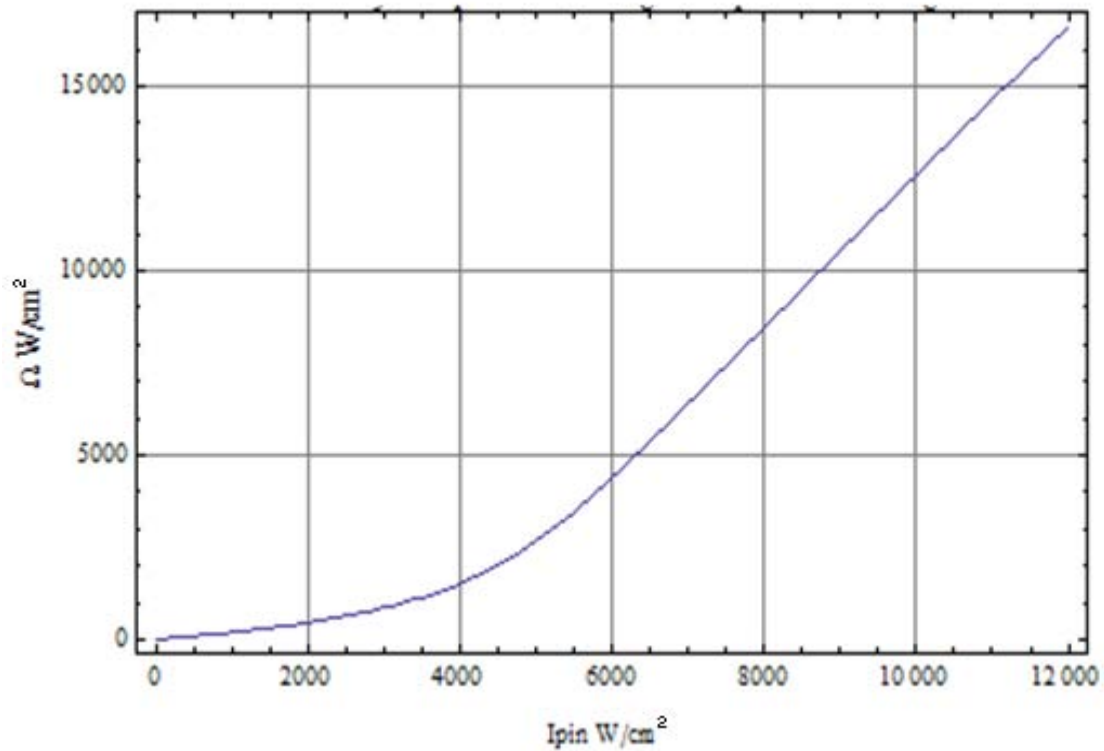


**Figure 16. Intracavity Pump Intensity – Frequency Independent**

The dramatic effect that varying ethane concentration has on output intensity and slope efficiency is readily seen in Figure 17 shown here:

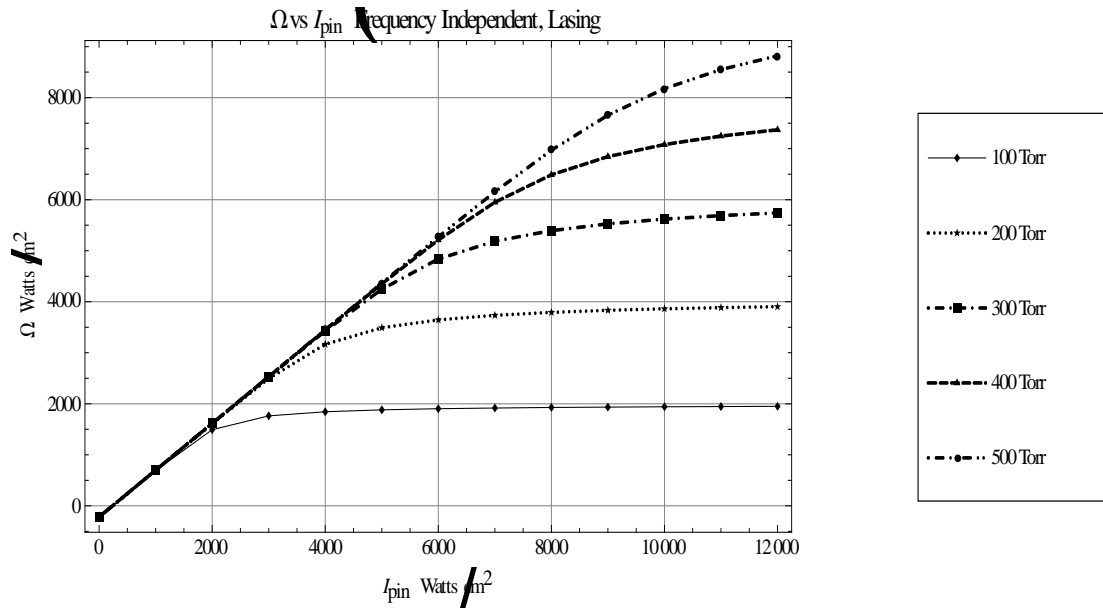


**Figure 17. Ethane Variation – Frequency Independent**

As seen, once the maximum spin-orbit relaxation rate is reached rapid rollover begins as the cyclic photon engine begins to break down, and bottlenecking in the upper pump state occurs. While increasing the buffer gas pressure seems like the apparent solution, broadening rates on the cross-sections must be considered and maintaining a single mode laser intensity becomes more challenging as more and more modes rise above threshold. There is also potential for cross-section overlap at high enough pressures which would greatly reduce efficiency of the ability to lase.

As an inverse, consider holding the ethane pressure a constant and varying alkali concentration. In doing so similar results are produced as can be seen on Figure 18 presented here:

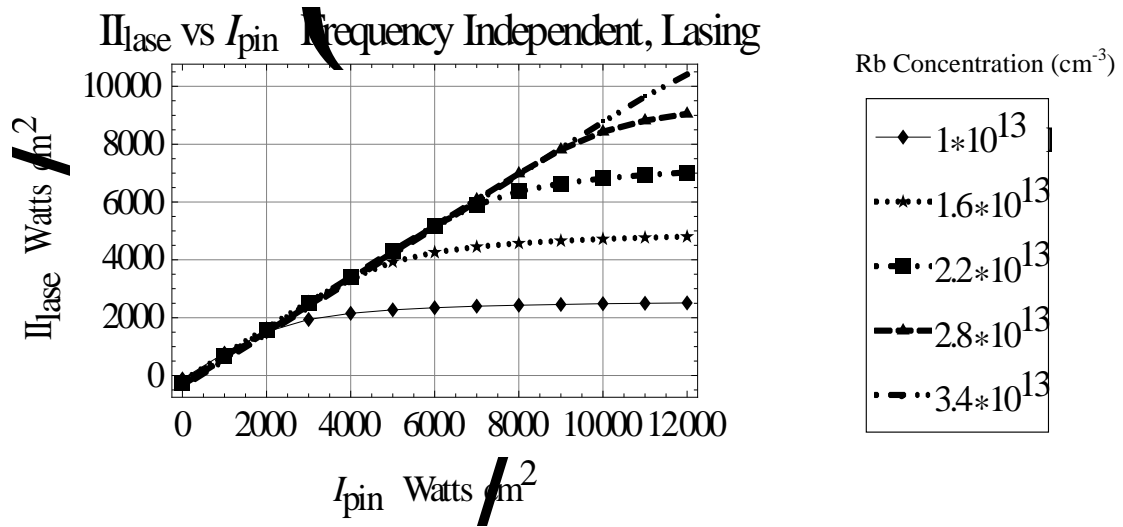


**Figure 18. Rubidium Variation – Frequency Independent**

When the alkali number density is low, the cell becomes easily bleached by the incident pump beam and the majority of the incident photons are wasted. However, the Q2L limit is maintained at higher input beam intensities and a linear slope efficiency maintained. The concentrations are not so optically thick as to limit lasing at such high pump intensities.

Window transmittivity also plays a vital role in slope efficiency. Gain is dependent on the negative of the log of the transmission factor, implying that as transmittivity increases, gain becomes more negative.

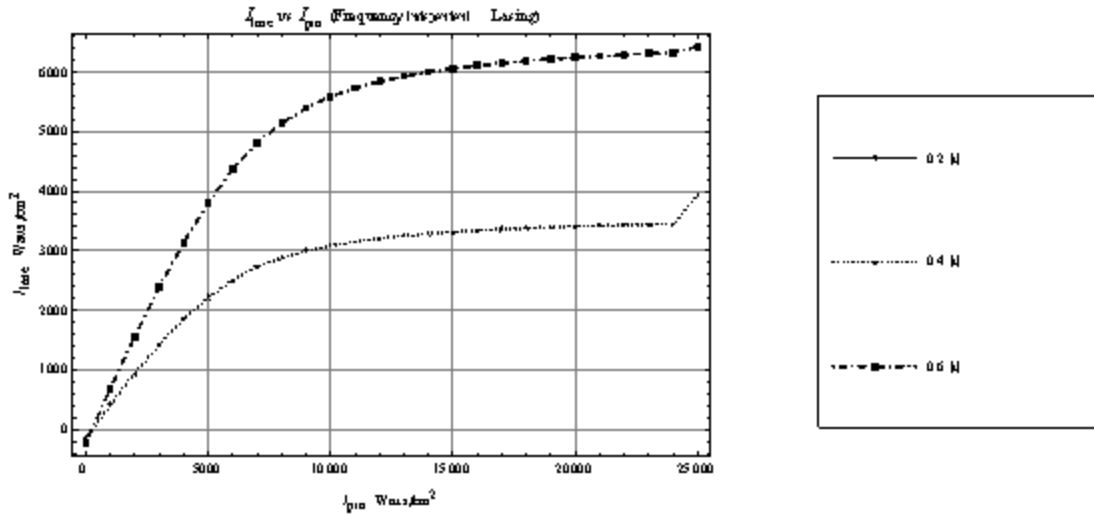


**Figure 19. Transmittivity Variation – Frequency Independent**

It is evident that Brewster windows and other transmission boosting design elements will play a critical role in optical-optical efficiency.

Cell Length is easily characterized and the optimal length is where the final round trip value of  $I_{pin}$  approaches zero. Figure 20 at the top of the following page shows the rapid rollover in slope efficiency as the cell becomes bleached by high pump intensities. It shows that the longer the cell, the longer the slope efficiency stays linear and relatively high. This is attributed to the idea that the pump beam becomes more dispersed throughout a larger medium and therefore less radiation is incident per photon. This reduces absorption on the pump transition, allowing for the buffer gas to stay ahead of the game and within the Q2L regime.

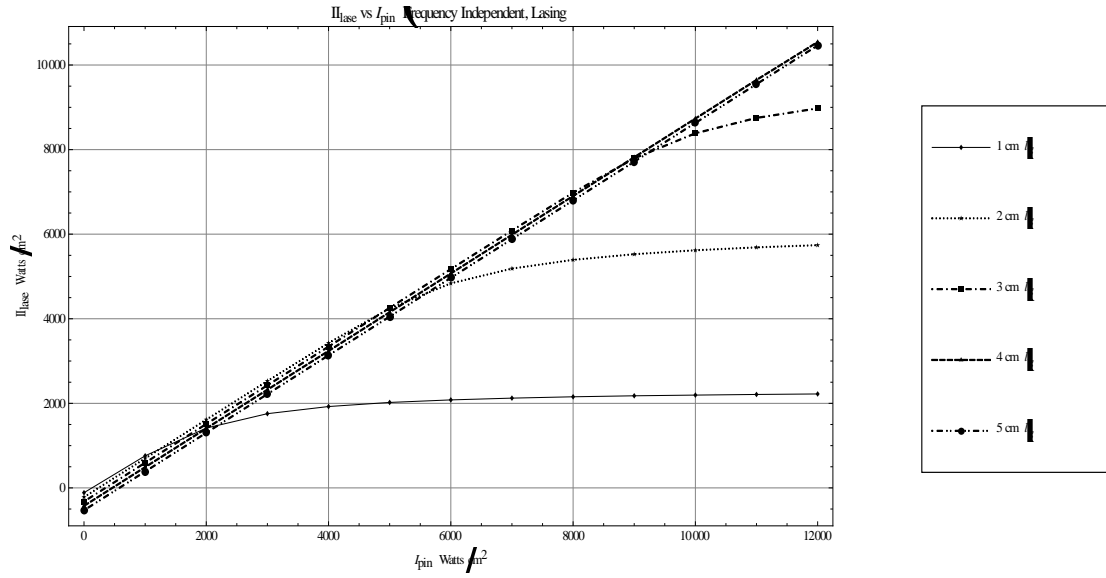


**Figure 20. Cell Length Variation – Frequency Independent**

### Broadband Pump, Lasing Mode Results

With confidence in the single frequency model the addition of pump bandwidth has been made and the results are shown here. Consider first only varying pump beam bandwidth. It is apparent from Figure 21 on the following page that matching the bandwidth to the absorption has a strong effect on optical-optical efficiency. It also has effects on the rollover point, population inversion and 3D plots showing the effects of bandwidth on the other parameters are analyzed. Comparison to the single frequency case shows a reduction in efficiency as expected. The graph on the following page gives our frequency dependent pump beam intensity as a function of  $I_{pin}$  for a range of spin-orbit pressures.

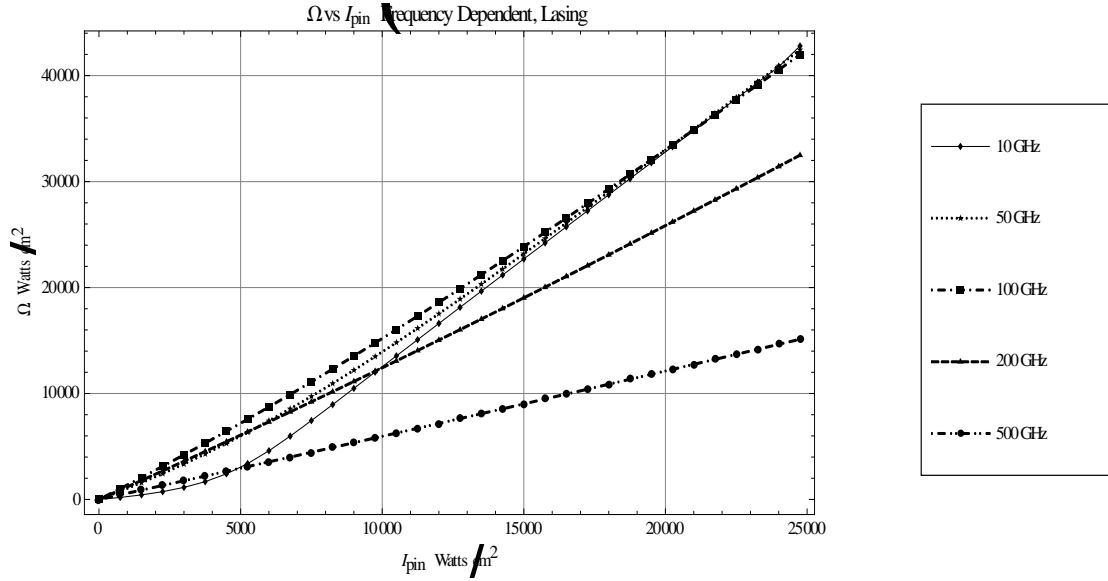


**Figure 21.  $\Omega$  vs  $I_{pin}$  – Frequency Dependent**

The highest bandwidth (500 GHz), has relatively low slope efficiency as a somewhat small proportion of the photons are within the absorption profile of the transition. As bandwidth decreases, slope efficiency rises. This is caused by the increase in absorption and a more rapid approach to the bleached transition limit. As you can see, the 10 GHz pump beam mimics the single frequency case in that around 5200 W/cm<sup>2</sup> the cell becomes bleached and  $\Omega_f$  approaches its limiting value of  $2I_{pin}$ . However, all other bandwidths excluding the 500 GHz have intracavity pump beam intensities greater than  $I_{pin}$ , implying that absorption towards a saturated state is consistent with those bandwidths. Given that more broadened pump beams can saturate the D<sub>2</sub> transition, there may be less of a demand to pursue narrowbanded diode stacks. An investigation into overall efficiency between narrowbanding the diode bars or pumping broadband may prove worthwhile. A second plot emphasizing the importance of spectral overlap is seen at the top of the following page.

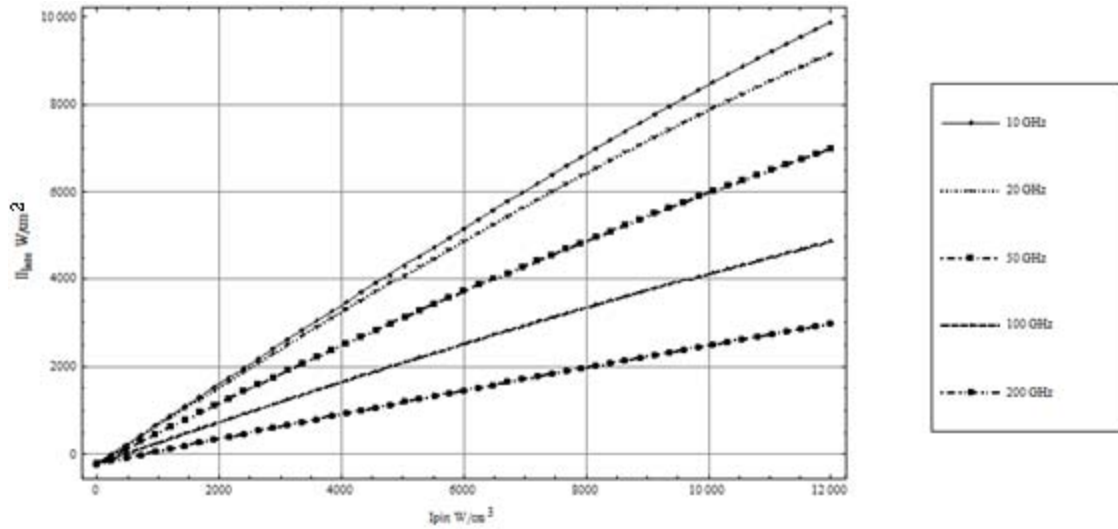


**Figure 22.  $I_{lase}$  vs  $I_{pin}$  – Frequency Dependent**

Figure 22 illustrates the importance of spectral overlap. This chart was produced with 600 Torr of ethane in order to ensure the results stayed in the Q2L limit. It shows the output laser intensity as a function of input beam intensity with FWHM's ranging from the absorption cross-sections FWHM of 10 GHz, up to 200 GHz. As is apparent, without a tight Gaussian pump beam efficiency is drastically reduced and net output power greatly diminishes. As bandwidth increases, more and more photons lie outside of a significant absorption probability, causing not only wasted incident radiation but polluting the cavity with extraneous energy potentially leading to thermal aberrations in the gain medium.

As bandwidth increases and absorption declines the Q2L limit is extended beyond its single frequency point. This is most evident through a comparison of Figures 22 and 23 on the following page and Figure 17. They are the same plots except Figure 17 is the single frequency case. Figure 22 has a Gaussian pump beam with a FWHM of 19.73 GHz, while Figure 23 has a FWHM of 200 GHz.



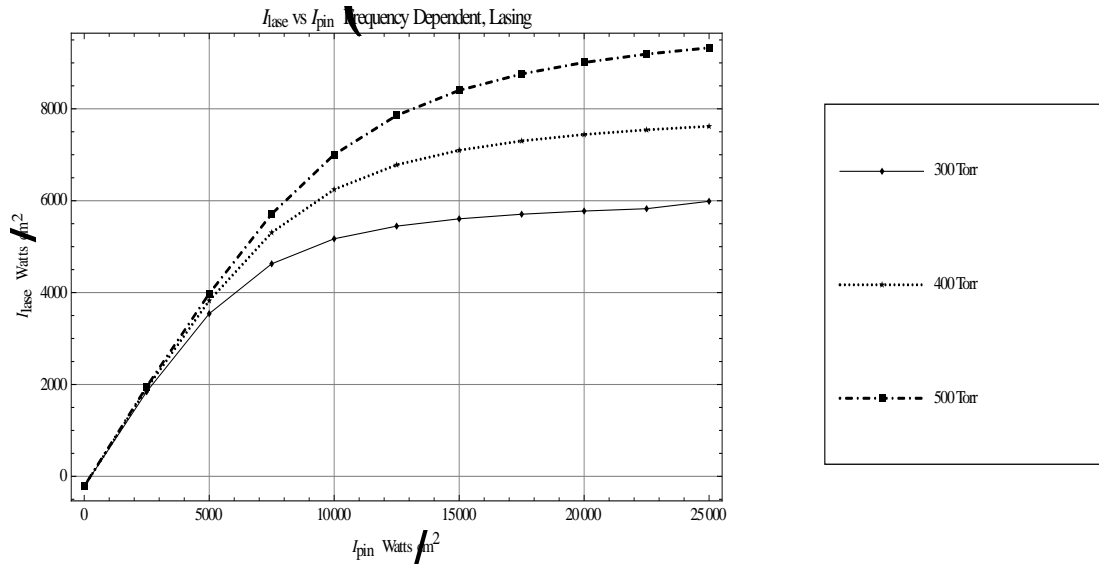


**Figure 23. Ethane Variation – Frequency Dependent (19.73 GHz)**

Shown above are the effects of ethane concentration on output intensity for a 19.73 GHz input beam. Through comparison with Figure 17, it is shown that the linear slope efficiency is maintained for larger values of  $I_{pin}$ . This is due to the reduction in absorbed beam intensity as bandwidth is increased. This can be seen to an even greater extent in Figure 24 below (200 GHz input beam bandwidth):

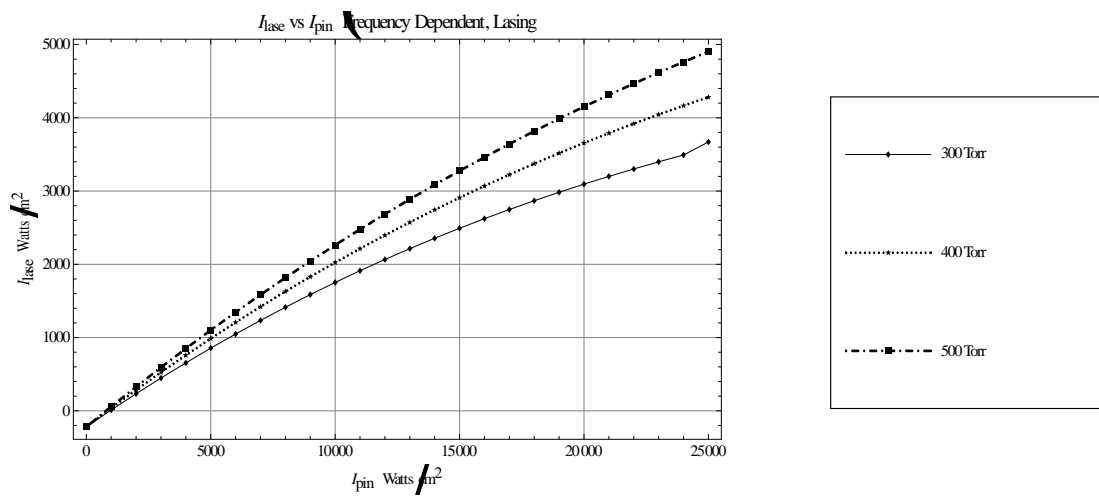


**Figure 24. Ethane Variation – Frequency Dependent (200 GHz)**

The reflectivity of the cavity at the lasing wavelength seems to play a rather insignificant role in output beam intensity. This may be attributed the extremely high gain nature of the alkali gain medium and its ability to reach threshold regardless of cavity reflection. The only obvious yet significant effect is seen when  $r = 1.0$ , or complete reflection back into the cavity. This result strengthens the confidence in the model as another intuitive result is produced as expected. Figure 25 show output intensities for reflectivities ranging from 0.2 – 0.5. The zero output intensity straddles the axis and is unseen but present on a color graph.

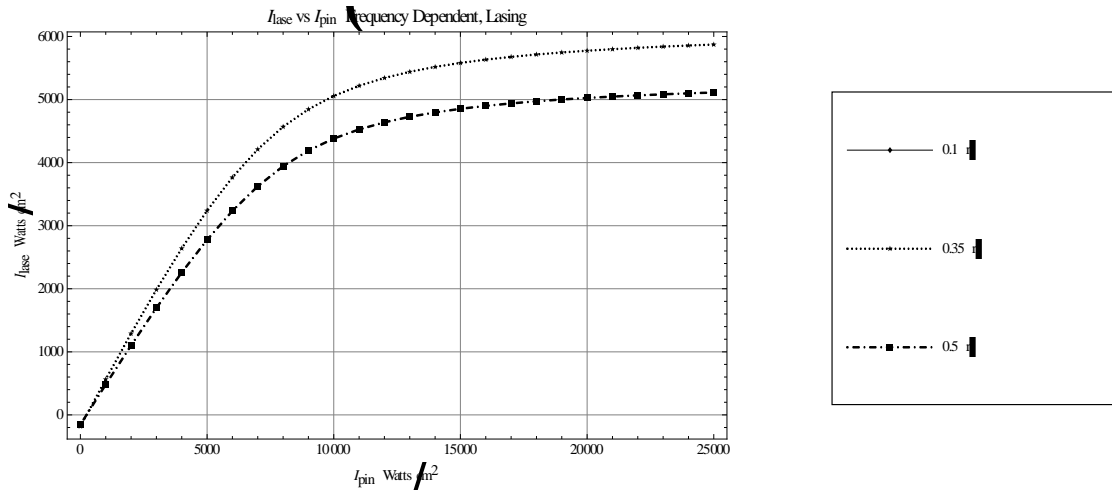


**Figure 25. Reflectivity Variation – Frequency Dependent**

As seen, reflectivity within the cavity slightly effects slope efficiency. It does not seem to effect the rollover effect or even maximize output beam intensity. This strengthens the idea that the key rate or dynamic of the system is the spin-orbit relaxation rate.

With this in mind a new parameter,  $\Delta$ , is defined as  $N_3/N_2$ . It represents how close the upper two laser levels are to their Boltzmann Distribution, or how close the system is to operating in the Q2L regime. To see how the pump bandwidth effects this ratio, a 3D contour plot with  $\Delta\nu_{pump}$  and  $I_{pin}$  as the independent variables is generated and shown below. The upper bound to the Boltzmann Equilibrated ratio for baseline parametric settings is set at  $\Delta = 1.73$ .

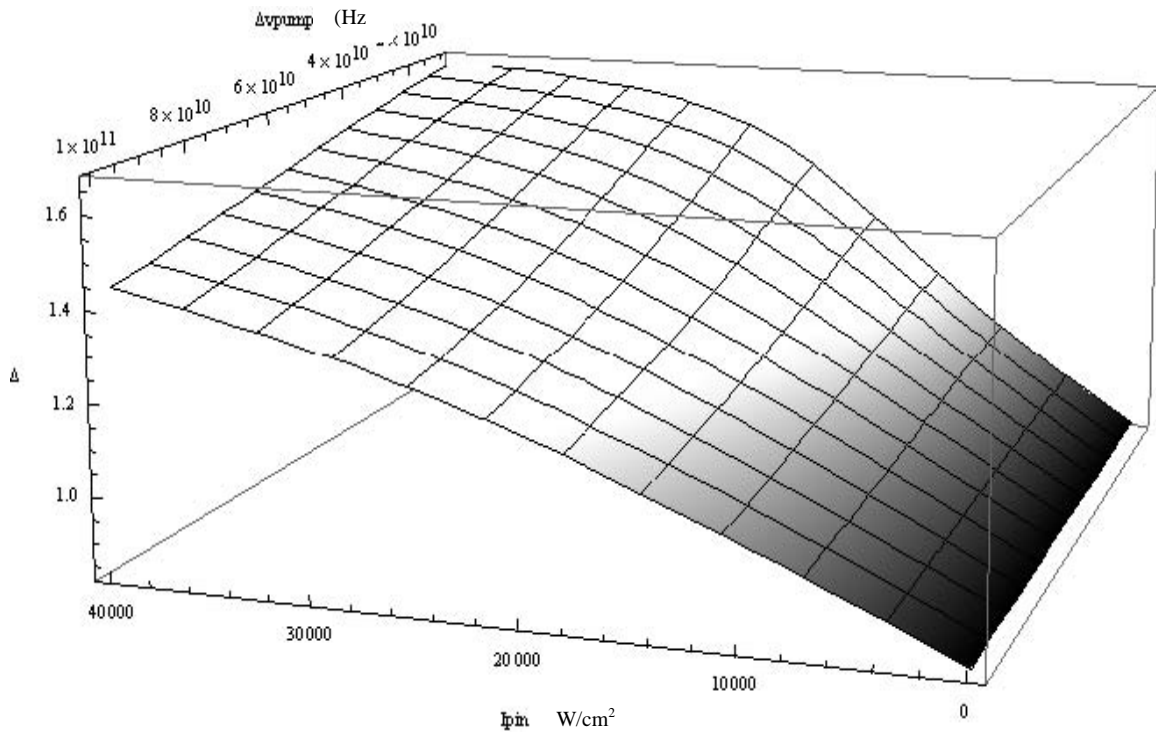


**Figure 26.  $\Delta$  -Bandwidth Variation – Frequency Dependent**

As seen pump bandwidth plays a significant role in defining  $\Delta$ . At lower bandwidths,  $\Delta$  rises more quickly as expected through a higher net absorption. It continues to stay above higher bandwidth values for the same pump intensity but rises more slowly as  $\Delta$  approaches its upper limit. This may be attributed to the decreased

percentage of the populations out of equilibrium which may reduce the buffer gas effective equilibrium rate. At high pump bandwidths the rise in  $\Delta$  is linear corresponding to the Q2L regime. In this case as more photons are absorbed into the upper lasing level there are more opportunities for the buffer gas to equilibrate with the alkalis in this state. It also shows that this rate is able to keep up with the stimulated emission rate on the lasing transition.

While the 2D plot of reflectivity suggested a weak dependence between output intensity and reflectivity, the contour plot below suggests that a lower reflectivity produces a higher output laser intensity. It shows that as reflectivity drops output intensity rises in a non-linear fashion.

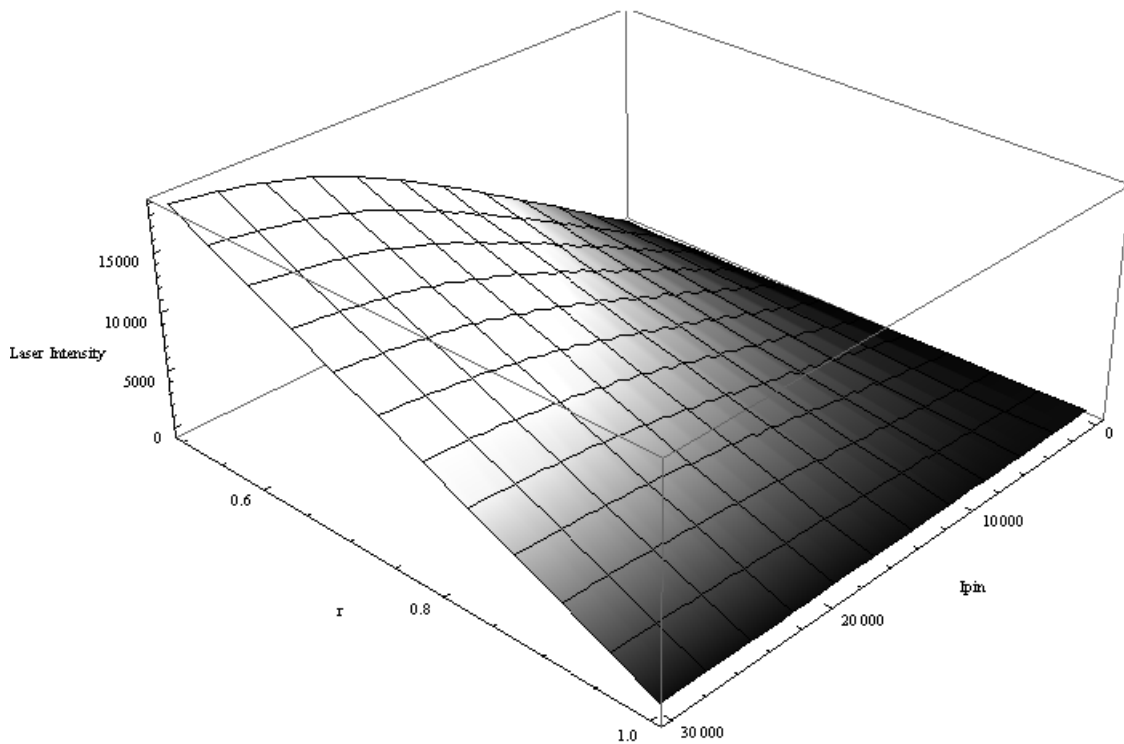


**Figure 27. Reflectivity Variation 3D – Frequency Dependent**

As seen maximum laser intensity is achieved at zero reflectivity. This once again suggest alkalis possess extremely high gain and a single ASE output beam maybe be capable of producing higher intensities than an oscillating laser cavity. However, for high beam quality a proper single mode resonator should be designed with a relatively low reflectivity.

Parametric efficiency studies have been conducted generating DPAL efficiency plots for a range of input beam strengths, buffer gas concentrations and pump beam bandwidth. Figure 25 below represents the optical-optical efficiency for a DPAL operating with a 10 kW input beam, 300 Torr of Ethane and 50 Torr He. The results incorporate the broadening rates recently published by Pitz *et al.*

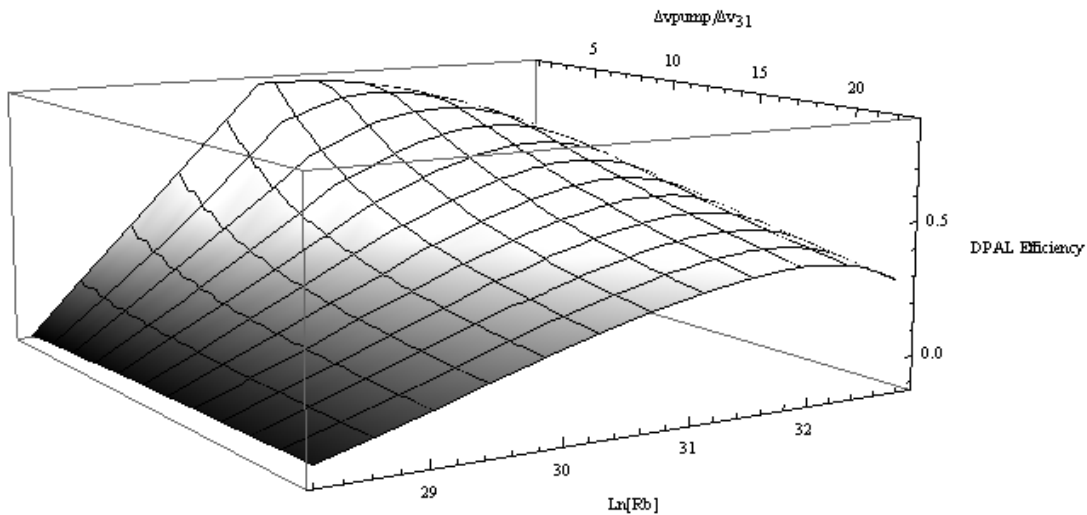


**Figure 28. DPAL Efficiency – Frequency Dependent**

DPAL efficiency is plotted against the natural log of the Rb concentration and the ratio between the pump and absorption cross section bandwidth. As expected, efficiency depends highly on bandwidth. This graph also shows the effects of high Rb concentration

on output. At the lower Rb concentrations, the pump beam is fully absorbed and slope efficiencies are linear and high for each given bandwidth. Near the center value of the Rb concentration efficiency drops as the gain medium becomes optically thick for a 10 kW input beam. This rollover however occurs at higher and higher Rb concentrations as bandwidth is increased, as expected.

As mentioned above reflectivity plays a key role in determining output beam strength. Presented below are the output intensities for a 80 kW input beam at various bandwidths. Once again, as bandwidth rises, output drops.

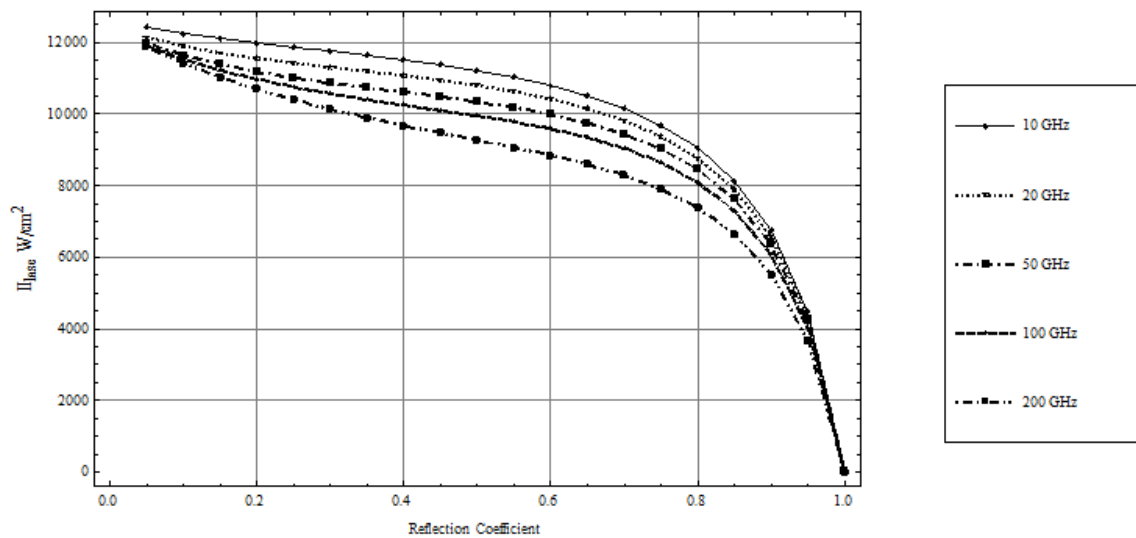


**Figure 29. Reflectivity Variation 2D – Frequency Dependent**

This plot reinforces the results of the 3D reflectivity contour plot above in that output intensity rises as reflectivity drops. However, eventually at high enough pump intensities these curves converge into a single line. This probably represents a pump beam intensity that bleaches the pump transition at all bandwidths. Figure 30 on the following page gives the output intensity vs reflectivity for a 100 kW input beam, and

shows this effect. The model uses a baseline value for cavity reflectivity of 0.2, corresponding to an efficiently designed laser system. At  $r = 0.2$ , there is still high output intensities but with the ability to potentially create a resonating, single mode, diffraction limited output beam.

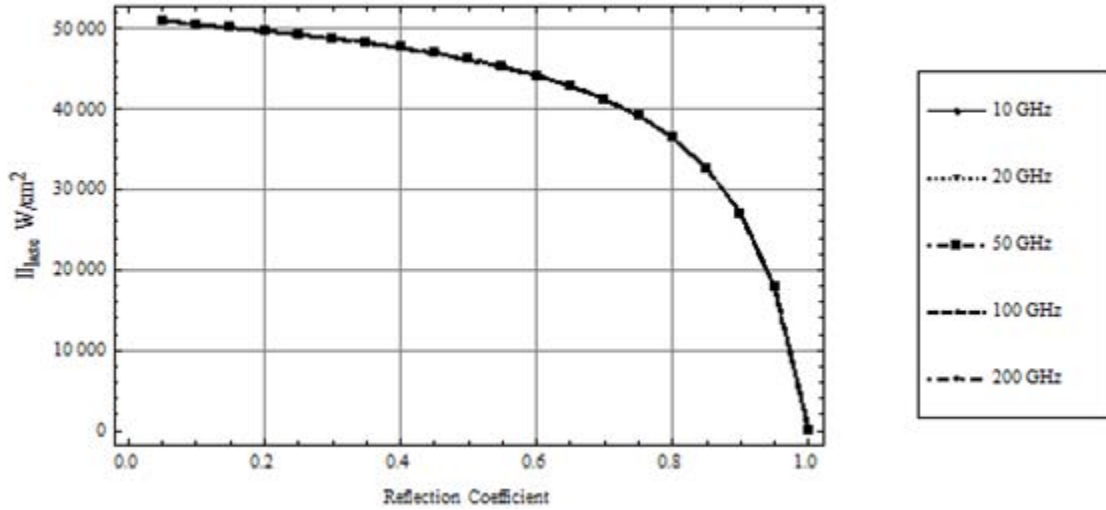


**Figure 30. DPAL Efficiency – Frequency Dependent**

As seen, at high pump intensities, the effects of bandwidth become insignificant due to saturation. This effectively reduces the system to is frequency independent model and solutions converge upon the lowest bandwidth instance.

One particular value of interest when analyzing pump bandwidth effects on laser performance is the ratio between the frequency independent intracavity pump beam intensity ( $\Omega$ ) and the frequency dependent intracavity pump beam intensity ( $\Omega_f$ ).

Explicitly, Gamma is defined as:

$$\Gamma = \frac{\Omega}{\Omega_f} \quad (36)$$

Intuitively one would believe that the frequency independent intracavity pump beam intensity is bounded to be always greater than the frequency dependent case. However, upon execution of the code the results are somewhat counter-intuitive. Figure 31 Gamma at a variety of pump bandwidths for the baseline parametric settings.

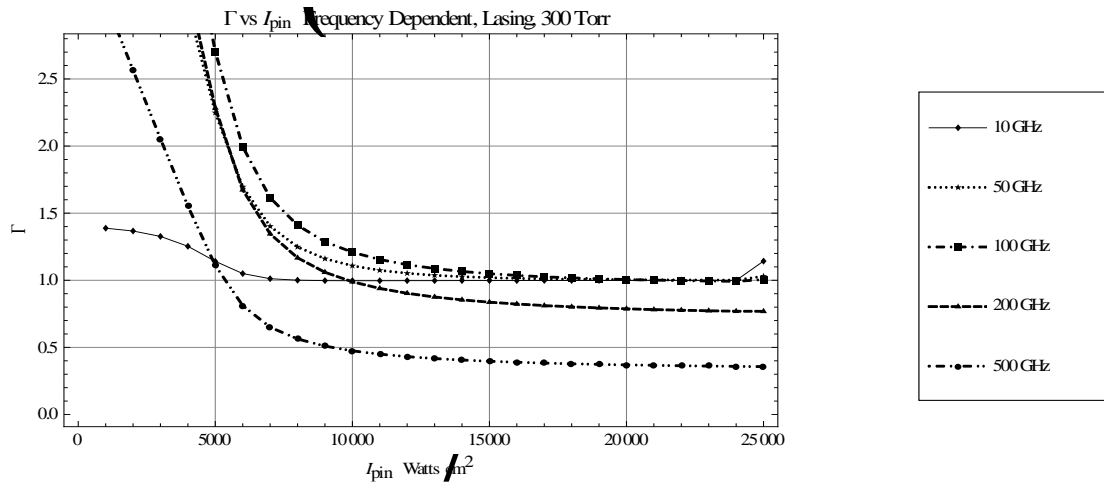


**Figure 31. Gamma – 300 Torr Ethane**

And the same plot again for a more pressurized (500 Torr) gain cell:

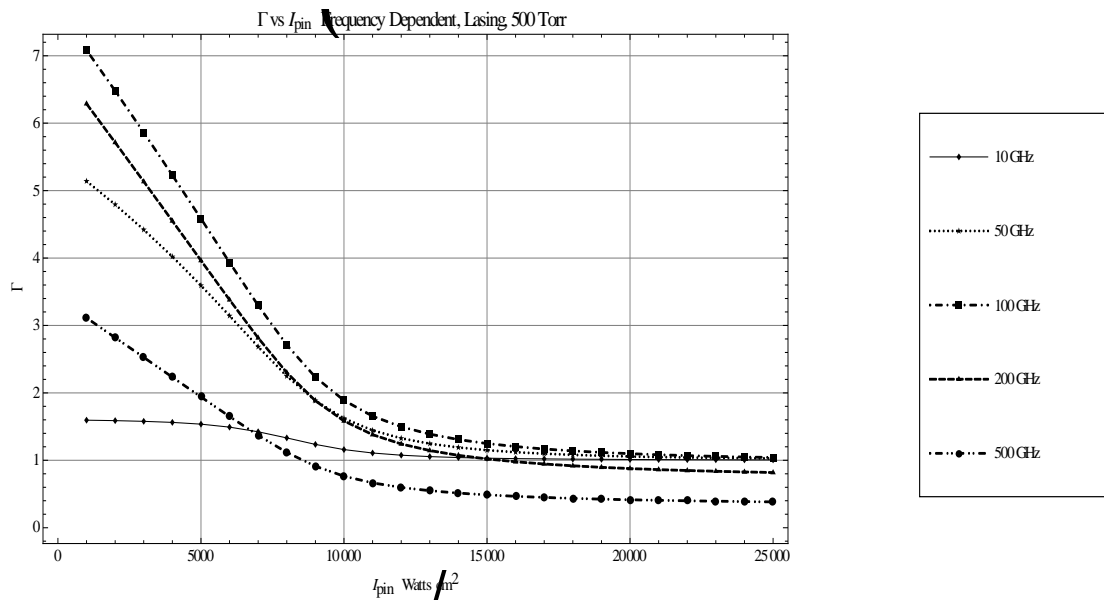


**Figure 32. Gamma – 500 Torr Ethane**



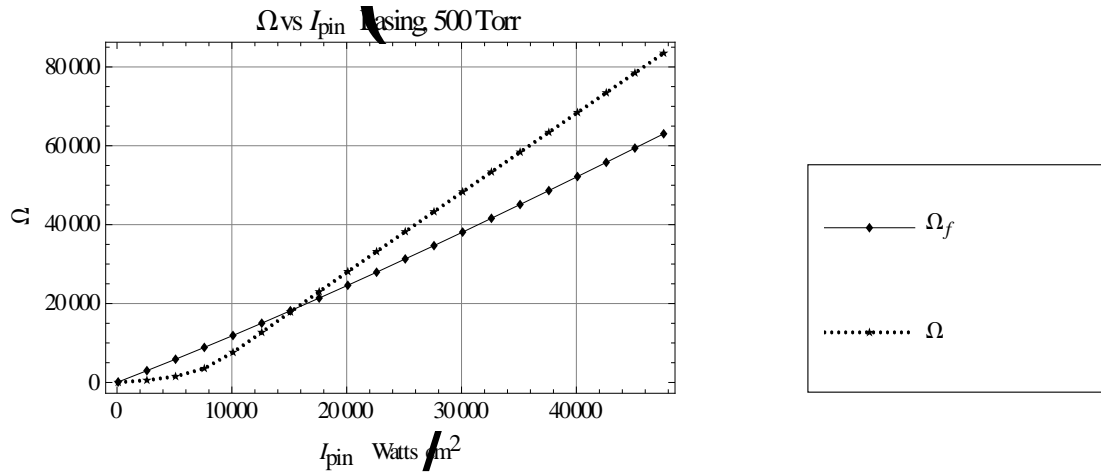


Figure 33 -  $\Omega$  vs  $I_{pin}$  500 Torr Ethane (500 Ghz)

Figure 33 shows the cause for Gamma dropping below 1. Initially the broadband pump has a greater slope efficiency, caused by a reduction in absorption. However, at higher pump intensities and saturated transition conditions the single frequency case approaches its intracavity slope limit of  $2I_{pin}$ , while the broadband case maintains a lower slope. At around  $15000 \text{ W/cm}^2$  the single frequency rate has bleached the transition whereas the broadband case has not, leading to a greater slope efficiency. Returning again to laser intensity, Figure 34 shows output intensity as a function of Rb concentration for a set of pump bandwidths:

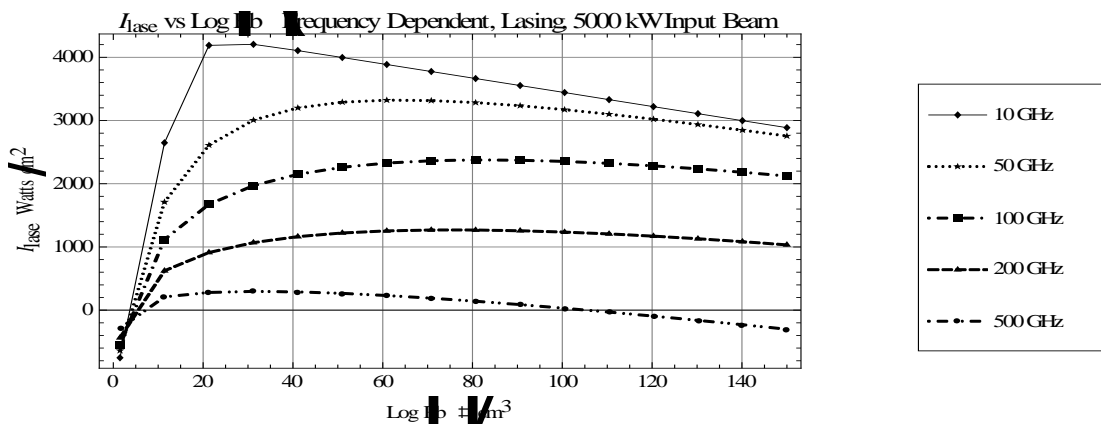
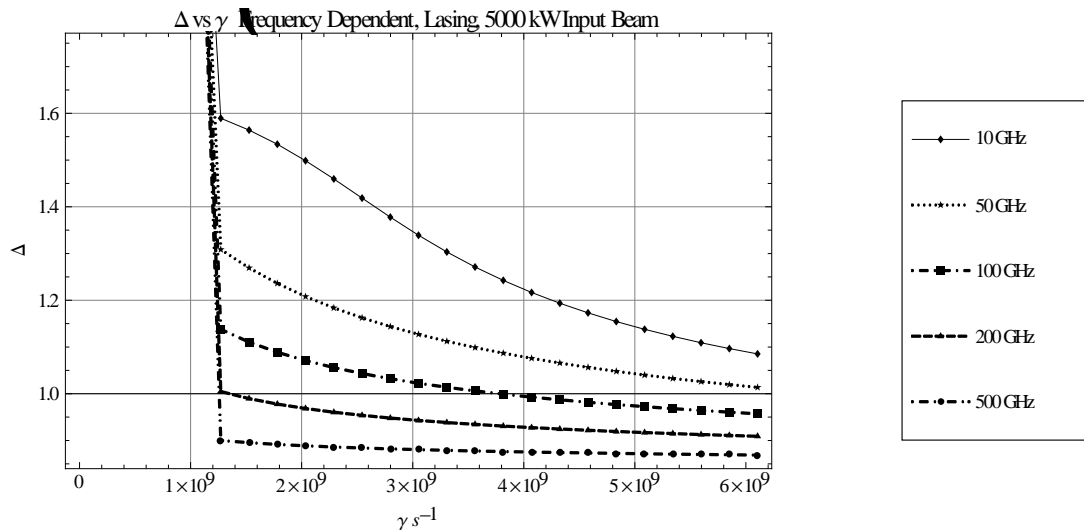


Figure 34.  $I_{lase}$  vs.  $\text{Log}[\text{Rb}]$  – 500 Torr Ethane

As is apparent in the graph, there is an optimal combination of alkali concentration, and bandwidth which maximizes output and this combination points directly at low bandwidth. At any given Rb concentration, the lowest bandwidth has the highest output intensity, and at 10 GHz the appropriate Rb concentration results in an optical to optical efficiency of about 80%. A second plot of  $\Gamma$  vs  $\gamma$  for a family of pump bandwidths is shown at the top of the following page. In order for the pump beam to drive the system it must excite quicker than the lasing beam relaxes. In order to do so it must get absorbed which is evident in Figure 34. At lower bandwidths  $\Delta$  maintains an inversion and there is bottlenecking at the upper pump state. This is a potential source of inefficiency and further studies of a  $\Delta$  for max efficiency may prove beneficial.



**Figure 35.  $\Delta$  – 300 Torr Ethane**

As shown,  $\Delta$  decreases as the spin orbit rate increases, or as Ethane is added to the system. A low  $\Delta$  is good for efficiency but one that is too low may limit laser performance.

The model is capable of producing a variety of results that can be used to analyze and more intuitively understand the dynamics and various interactions of the system. By accurately predicting the output beam intensity based on the fundamental elements of any laser system, parametric solutions can be obtained upon which engineers can base their designs.

## V. Conclusions and Discussion

With the results of the model readily available and interpretable, conclusions on the effects of broadband pumping are made. Also discussed are various effects between the other independent variables. Third, issues with the approximations made are addressed and finally, suggestions for future work on the model are made.

In essence, a broadening of the pump bandwidth offers very little towards achieving maximum laser performance. As seen, as bandwidth increases, output laser intensity decreases. Given that an objective of the DPAL is cost efficiency and low power-usage, maximizing pump absorption is critical. However, the model does show that a very high efficiency is theoretically possible, (albeit an engineering feat yet to be seen). There are also certain cases where it may be possible for a more broad banded beam to actually be more efficient, as is seen in Figure 21.

While it may seem intuitive, in a quantum mechanical sense, that any broadening of an energizing spectral source will reduce efficiency, the current state of affairs regarding diode stacks puts their bandwidths in the 100's of GHz. With this in mind, if demand for output power begins to heavily outweigh efficiency concerns, systems can be designed based on the appropriate pump beam interaction, allowing the model to "pave the way" for future progress. The model is also an open book without an ending and is capable of become far more robust, accurate, precise and efficient.

As seen throughout the data, there must be a merger between all system parameters in order to maximize performance. However, it was shown that some variables have a greater influence than others. For example, reflectivity plays a minor role in determining overall performance whereas buffer gas concentrations are far more critical. Bandwidth

plays a significant role however in practicality it seems as if it would be easier to simply increase the pump intensity rather than adjust the ethane concentration. Cell length in the standard DPAL design is held constant and the various other parameters can be adjusted to make the most out of any length cell. In this author's opinion, the system primarily comes down to alkali and buffer gas concentrations, and pump beam intensity.

While the model is quasi-analytic, founded in laser engineering, and compares well with experimental data, it lacks a sense of completeness or of an all encompassing simulation of a true laser system. In a way, it is an algorithm reduced to the key elements of any laser system, a simplification, an "ideal" representation of a far more detailed phenomenon. Of greatest concern is the idea that all the alkalis reside in one of only three possible states ( for Rb:  $5^2P_{3/2}$ ,  $5^2P_{1/2}$  or  $5^2S_{1/2}$ ). Recently collected data suggests that alkali's, upon being excited to the  $5^2P_{3/2}$  state experience a myriad of kinetic processes and excitations before fluorescing back to ground. This results in "spreading out" of the alkalis atoms into the various electron states. Fluorescence of a laser pumped, vacuum sealed, thermally insulated Rb cell was collected by means of an optical cable and a 0.3 M spectrometer. A series of data collections were undertaken to observe the intensity fluctuations of the various Rb emission lines as a function of Rb concentration and incident beam intensity. For each set the Rb vapor was subject to high intensity, pulsed radiation in resonance with the  $D_2$  transition. A Grotrian Diagram displaying the various observed emission lines is shown on the following page.

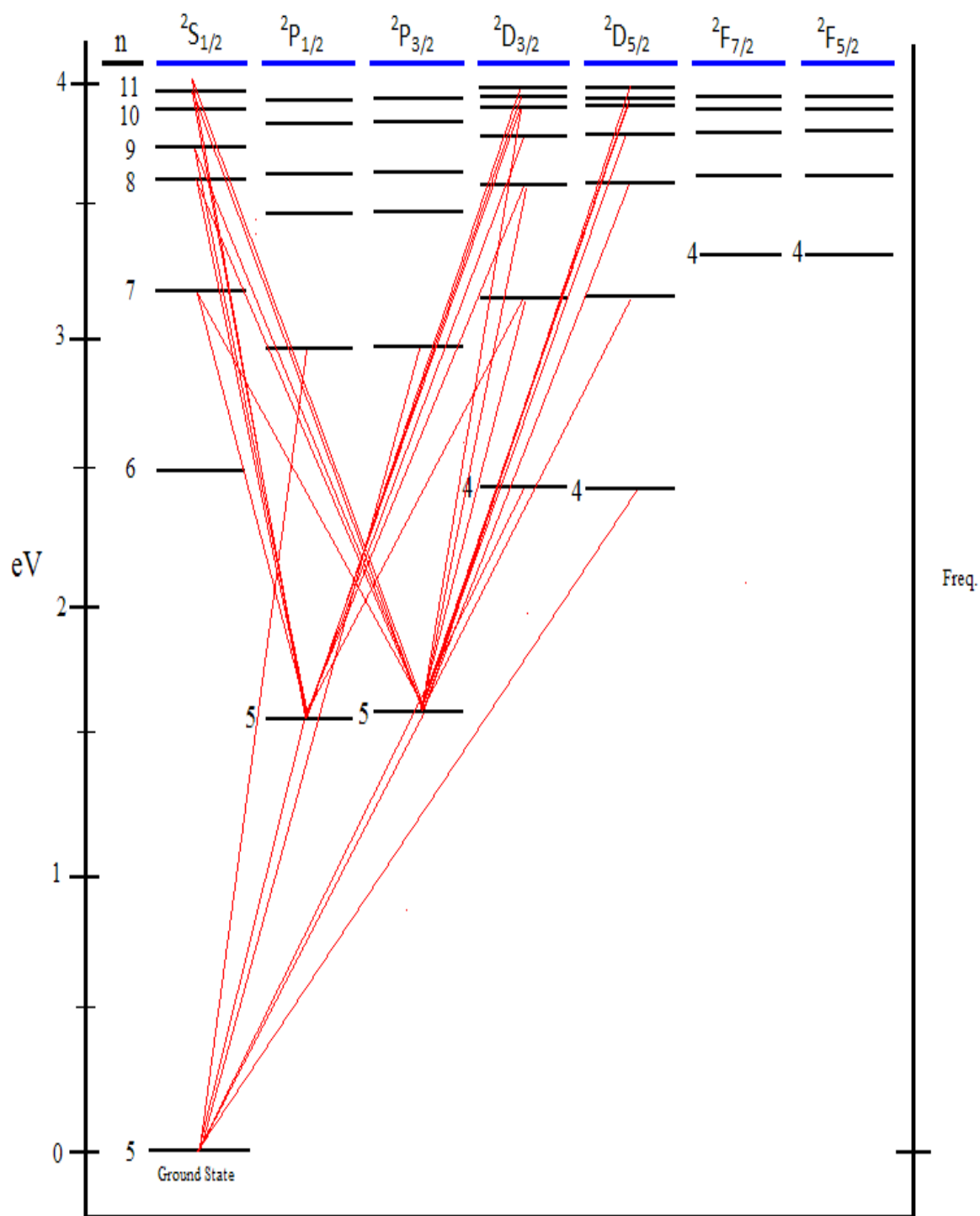


Figure 36. Grotrian Diagram – Laser Pumped Rb Fluorescence

As one can see, many different energy levels become populated solely from pumping on the  $D_2$  line. A closer inspection of Figure 29 reveals that all dipole allowed transitions are observed and even some non-dipole allowed. A detector with a larger bandwidth may reveal even more Rb emissions.

A second issue with the model is that it makes great strides in an effort to maintain its quasi-analytic nature. However, at times, this author feels too much of the physical phenomena occurring in the laser system is ignored or deemed insignificant. In the derivations of the longitudinally averaged two way intracavity pump beam intensity certain terms are ignored or neglected for simplicity. This author suggests that one should take advantage of the computational power accessible by AFIT and other facilities to produce a more thorough account of the interactions within the system.

Even so, the model still makes accurate predictions and encompasses all of the fundamental laser physics involved with the DPAL. It is an excellent tool for analysis, exploration, brainstorming, and there are many upgrades that could begin tightening the gap between the model and the lab. First, extending the frequency dependence of the pump transition to the lasing transition would produce more accurate and fundamentally sound results. Second, considering numerical integration is already implemented in the code, a more precise and approximation free definition of the various system variables may open up new phenomena or unforeseen issues within the system. For user-friendliness, implementing the code into a compiled language would dramatically reduce runtime. The closer the model represents reality, the closer it will predict it.

## Appendix A

### Rubidium Physical Data:

#### Physical data

##### Electronic data

**Shells:** 2,8,18,8,1  
**Orbitals:** [Kr] 5s<sup>1</sup>  
**Electronegativity:** 0.9, 0.8  
**1. Ionization potential:**  
 4.1771 eV  
**2. Ionization potential:**  
 27.28 eV  
**3. Ionization potential:** 40.0  
 eV  
**Oxidation states:** 1

##### Thermal data

**Melting point:** 38.89 °C  
**Boiling point:** 686 °C  
**Specific heat:** 0.363 J/gK  
**Heat of fusion:** 2.192 kJ/mol  
**Heat of vaporization:** 72.216  
 kJ/mol  
**Thermal conductivity:** 0.582  
 W/cmK

##### Steric data

**Atomic radius:** 2.98 Å  
**Ionic radius:** 1.61 Å  
**Covalent radius:** 2.16 Å  
**Atomic volume:** 55.9 cm<sup>3</sup>/mol  
**Density (293 K):** 1.53 g/cm<sup>3</sup>  
**Crystal structure:** Cubic: Body  
 centered

#### Isotopes

Nuclide	Abundance [%]	Mass	Spin	Halflife	Decay mode
<sup>81</sup> Rb	0	81	3/2	4.57h	EC, β <sup>+</sup>
<sup>82</sup> Rb	0	82	1	1.258m	β <sup>+</sup> , EC
<sup>83</sup> Rb	0	83	5/2	86.2d	EC, EC
<sup>84</sup> Rb	0	83.914	2	32.9d	EC, β <sup>+</sup> , β <sup>-</sup>
<sup>85</sup> Rb	72.15	84.9118	5/2	--	Stable
<sup>85</sup> Rbm	0	85	0	>1μs	IT
<sup>86</sup> Rb	0	85.911	2	18.65d	β <sup>-</sup> , EC
<sup>87</sup> Rb	27.85	86.9092	3/2	4.8E10y	β <sup>-</sup>
<sup>88</sup> Rb	0	88	2	17.7m	β <sup>-</sup>
<sup>89</sup> Rb	0	89	3/2	15.44m	β <sup>-</sup>
<sup>90</sup> Rb	0	90	1	2.6m	β <sup>-</sup>
<sup>90</sup> Rbm	0	90	4	4.3m	β <sup>-</sup> , IT



## Appendix B - Simulation Code (Three Level Laser System)

Presented here is a Brief Mathematica Tutorial and a concisely annotated computer simulated model for The Diode Pumped Alkali Laser.

### Mathematica Tutorial :

This tutorial will focus on the necessities of executing the code.

#### 1.) Cell Evaluation :

On the far right of each window are small "Cell" dividers and allow one to select a cell by left clicking on the divider. Once selected, hit either the enter key on the number pad or shift + enter. Do not evaluate cells containing notation.

#### 2.) Execution of Code :

a.) First select a section of code tailored to your analysis goals (i.e. - if you want to do frequency independent analysis, select one of the frequency independent sections of the appendix below)

b.) Once selected, input all user dependent variables into the "System Parameters" subsection.

c.) After completely defining all parametric values, evaluate all cells not consisting of notation.

d.) At the end of each section is a rubrick giving an outline of how to generate plots corresponding to that section. Simply input the user specified plot range and independent variable and execute the cell.

#### 3.) Generating Black and White Plots with Markers and Legends :

To generate sophisticated plots capable of describing more data simultaneously utilize the "MultipleListPlot" function. This function is capable of generating marker points for each data point and a legend for each data set.

a.) Load graphics package (ignore error message) :

```
<< Graphics`MultipleListPlot`;
```

b.) Rubrick for generating Black and White Plots of multiple lines :

```
MultipleListPlot[
{Table1[{X - variable, Y - Variable}, {X, X - min, X - max, step - size}],
Table2[{X - variable, Y - Variable}, {X, X - min, X - max, step - size}],
Table3[{X - variable, Y - Variable}, {X, X - min, X - max, step - size}],
Table4[{X - variable, Y - Variable}, {X, X - min, X - max, step - size}]},
PlotLabel → "Insert Title", FrameLabel → {"X-Axis Label", "Y-Axis Label"},
GridLines → Automatic, Frame → True, FillingStyle → None,
PlotJoined → True,
PlotLegend → {Table1 label, Table2 label, Table3 label, Table4 label}]
```

#### 4.) Exporting data as a .dat file (ASCII)

To generate a file consisting of a table of the independent and dependent variables of a function utilize the "Export" function.

Example :

i.) Generate a Table :

```
Table1 = Table[{Ipin, 15*Ipin}, {Ipin, 0, 500, 10}]

{{0, 0}, {10, 150}, {20, 300}, {30, 450}, {40, 600}, {50, 750}, {60, 900},
{70, 1050}, {80, 1200}, {90, 1350}, {100, 1500}, {110, 1650}, {120, 1800},
{130, 1950}, {140, 2100}, {150, 2250}, {160, 2400}, {170, 2550}, {180, 2700},
{190, 2850}, {200, 3000}, {210, 3150}, {220, 3300}, {230, 3450}, {240, 3600},
{250, 3750}, {260, 3900}, {270, 4050}, {280, 4200}, {290, 4350}, {300, 4500},
{310, 4650}, {320, 4800}, {330, 4950}, {340, 5100}, {350, 5250},
{360, 5400}, {370, 5550}, {380, 5700}, {390, 5850}, {400, 6000},
{410, 6150}, {420, 6300}, {430, 6450}, {440, 6600}, {450, 6750},
{460, 6900}, {470, 7050}, {480, 7200}, {490, 7350}, {500, 7500}}
```

ii.) Export the table specifying save location and file type :

```
Export["C:\\Documents and Settings\\pjones\\Table1.dat", Table1]
```

C:\\Documents and Settings\\pjones\\Table1.dat

The file can be found at the file path given by the output.

This concludes the tutorial.

**\*\* NOTE \*\***

1. Each section is to be viewed as an independently operating simulation. Within each part is a complete system model.
2. Upon execution of any section ensure that all variables have been cleared by quitting the local Mathematica Kernel. This is accomplished by selecting the "Evaluation" menu button in Mathematica and then selecting "Quit Kernel."
3. User input variables have been cleared and inputs are to be specified under "System Parameters."

Ethane Number Densities (#/cm<sup>3</sup>) Corresponding to Various Pressures (Torr) :

100 Torr →  $3.22 \times 10^{18}$

200 Torr →  $6.44 \times 10^{18}$

300 Torr →  $9.66 \times 10^{18}$

400 Torr →  $1.28 \times 10^{19}$

500 Torr →  $1.61 \times 10^{19}$

#### Baseline Parametric Settings :

(Simply execute this segment if you wish to evaluate the code at its baseline operating conditions, and spectroscopic constants corresponding the the table found in Reference [])

```
h := 6.626068 * 10-34
t21 := 27.70 * 10-9
t31 := 26.23 * 10-9
σ21 := 4.80 * 10-13
σ31 := 4.92 * 10-13
k32 := 3.16 * 10-10
v31 := 3.845 * 1014
v21 := 3.774 * 1014
θ := 0.8670379156330899
gth[r_, t_, lg_] := -Log[r * t4] / (2 * lg)
k := 1.3806504 * 10-23
T := 300
c := 3.0 * 1010
λ31 := c / v31
λ21 := c / v21
M := 9.66 * 1018
ntot := 1.85 * 1013
lg := 2
r := 0.2
t := 0.975
γ := M * k32
```

Part 1 : Frequency Independent, No Lasing

(Assume steady state)

Rate Equations ( $\Psi = 0$ )

$$\text{Solve}\left[\begin{aligned}0 &== \sigma_{31} \star (n_3 - 2 \star n_1) \star \frac{\Omega}{h \star \nu_{31}} + \sigma_{21} \star (n_2 - n_1) \star \frac{\Psi}{h \star \nu_{21}} + \frac{n_2}{t_{21}} + \frac{n_3}{t_{31}}, \\0 &== -\sigma_{21} \star (n_2 - n_1) \star \frac{\Psi}{h \star \nu_{21}} + \gamma \star (n_3 - 2 \star \text{Exp}[-\theta] \star n_2) - \frac{n_2}{t_{21}}, \\0 &== n_1 + n_2 + n_3 - n_{\text{tot}}, \\0 &== \Psi\end{aligned}\right],$$

$$\{n_1, n_2, n_3\}$$

This solves for our population densities as a function of intracavity pump beam intensity :

$$\begin{aligned}n_1[\mathcal{Q}] &:= \frac{(n_{\text{tot}} (e^{\theta} h \nu_{31} + 2 h t_{21} \nu_{31} \gamma + e^{\theta} h t_{31} \nu_{31} \gamma + e^{\theta} t_{31} \sigma_{31} \mathcal{Q} + 2 t_{21} t_{31} \gamma \sigma_{31} \mathcal{Q}))}{(e^{\theta} h \nu_{31} + 2 h t_{21} \nu_{31} \gamma + e^{\theta} h t_{31} \nu_{31} \gamma + 3 e^{\theta} t_{31} \sigma_{31} \mathcal{Q} + 6 t_{21} t_{31} \gamma \sigma_{31} \mathcal{Q} + 2 e^{\theta} t_{21} t_{31} \gamma \sigma_{31} \mathcal{Q})} \\n_2[\mathcal{Q}] &:= \frac{(2 e^{\theta} n_{\text{tot}} t_{21} t_{31} \gamma \sigma_{31} \mathcal{Q})}{(e^{\theta} h \nu_{31} + 2 h t_{21} \nu_{31} \gamma + e^{\theta} h t_{31} \nu_{31} \gamma + 3 e^{\theta} t_{31} \sigma_{31} \mathcal{Q} + 6 t_{21} t_{31} \gamma \sigma_{31} \mathcal{Q} + 2 e^{\theta} t_{21} t_{31} \gamma \sigma_{31} \mathcal{Q})} \\n_3[\mathcal{Q}] &:= \frac{(2 n_{\text{tot}} t_{31} (e^{\theta} + 2 t_{21} \gamma) \sigma_{31} \mathcal{Q})}{(e^{\theta} h \nu_{31} + 2 h t_{21} \nu_{31} \gamma + e^{\theta} h t_{31} \nu_{31} \gamma + 3 e^{\theta} t_{31} \sigma_{31} \mathcal{Q} + 6 t_{21} t_{31} \gamma \sigma_{31} \mathcal{Q} + 2 e^{\theta} t_{21} t_{31} \gamma \sigma_{31} \mathcal{Q})}\end{aligned}$$

```

System Parameters :

h := 6.626068 * 10-34

t21 :=

t31 :=

σ21 :=

σ31 :=

k32 :=

v31 :=

v21 :=

θ := 0.8670379156330899

gth[r_, t_, lg_] := -Log[r * t4] / (2 * lg)

k := 1.3806504 * 10-23

T :=

c := 3.0 * 1010

λ31 := c / v31

λ21 := c / v21

M :=

ntot :=

lg :=

r :=

t :=

γ := M * k32

```

Defining our Two - Way Intracavity Longitudinally Averaged Pump Beam Intensity :  
(Frequency Independent)

$$\Omega\Omega[I_{pin\_}, \Omega] := \left( \frac{I_{pin}}{\sigma_{31} * (n3[\Omega] - 2 * n1[\Omega]) * lg} \right) * \\ (\text{Exp}[\sigma_{31} * (n3[\Omega] - 2 * n1[\Omega]) * 2 * lg] - 1)$$

$$\Omega[I_{pin\_}] := (\Omega /. \text{FindRoot}[\Omega\Omega[I_{pin}, \Omega] - \Omega, \{\Omega, (I_{pin})\}])$$

Rubrick for generating plots :

```
Plot[\Omega[I_{pin}], {I_{pin}, Minimum, Maximum}, GridLines -> Automatic,
Frame -> True, PlotLabel -> "Insert Title Here",
FrameLabel -> {"X-Axis Label", "Y-Axis Label"}]
```

Part 2 : Frequency Independent, Lasing

(Assume steady state)

Rate Equations ( $\Psi \neq 0$ )

$$\text{Solve}\left[\begin{aligned}0 &= \sigma_{31} \star (n_3 - 2 \star n_1) \star \frac{\Omega}{h \star \nu_{31}} + \sigma_{21} \star (n_2 - n_1) \star \frac{\Psi}{h \star \nu_{21}} + \frac{n_2}{t_{21}} + \frac{n_3}{t_{31}}, \\0 &= -\sigma_{21} \star (n_2 - n_1) \star \frac{\Psi}{h \star \nu_{21}} + \gamma \star (n_3 - 2 \star \text{Exp}[-\theta] \star n_2) - \frac{n_2}{t_{21}}, \\0 &= n_1 + n_2 + n_3 - n_{\text{tot}}, \\-\text{Log}[r \star t^4] / (2 \star \lg) &= \sigma_{21} \star (n_2 - n_1)\end{aligned}\right],$$

$$\{n_1, n_2, n_3, \Psi\} // \text{FullSimplify}$$

Defining our steady state lasing populations as functions of our input parameters :

$$\begin{aligned}n1[\varrho, n_{\text{tot}}, M, r, t, \lg] &:= \\&\frac{(2 h k_{32} M t_{31} \nu_{31} \text{Log}[r t^4] + e^{\theta} (h (\nu_{31} + k_{32} M t_{31} \nu_{31}) + t_{31} \sigma_{31} \varrho) (2 \lg n_{\text{tot}} \sigma_{21} + \text{Log}[r t^4]))}{(4 \lg \sigma_{21} (h k_{32} M t_{31} \nu_{31} + e^{\theta} (h (\nu_{31} + k_{32} M t_{31} \nu_{31}) + 2 t_{31} \sigma_{31} \varrho)))} \\n2[\varrho, n_{\text{tot}}, M, r, t, \lg] &:= \\&\frac{(e^{\theta} (2 \lg n_{\text{tot}} \sigma_{21} (h (\nu_{31} + k_{32} M t_{31} \nu_{31}) + t_{31} \sigma_{31} \varrho) - (h (\nu_{31} + k_{32} M t_{31} \nu_{31}) + 3 t_{31} \sigma_{31} \varrho) \text{Log}[r t^4]))}{(4 \lg \sigma_{21} (h k_{32} M t_{31} \nu_{31} + e^{\theta} (h (\nu_{31} + k_{32} M t_{31} \nu_{31}) + 2 t_{31} \sigma_{31} \varrho)))} \\n3[\varrho, n_{\text{tot}}, M, r, t, \lg] &:= \\&\frac{(t_{31} (2 \lg n_{\text{tot}} \sigma_{21} (h k_{32} M \nu_{31} + e^{\theta} \sigma_{31} \varrho) + (-h k_{32} M \nu_{31} + e^{\theta} \sigma_{31} \varrho) \text{Log}[r t^4]))}{(2 \lg \sigma_{21} (h k_{32} M t_{31} \nu_{31} + e^{\theta} (h (\nu_{31} + k_{32} M t_{31} \nu_{31}) + 2 t_{31} \sigma_{31} \varrho)))}\end{aligned}$$



Defining our Two - Way Intracavity Longitudinally Averaged Pump Beam Intensity :  
(Frequency Independent)

```
Q[Ipin_, ntot_, M_, r_, t_, lg_] :=
  (Q /. FindRoot[QQ[Ipin, Q, ntot, M, r, t, lg] - Q, {Q, (Ipin)}])

QQ[Ipin_, Q_, ntot_, M_, r_, t_, lg_] :=
  (Ipin / (σ31 * ((n3[Q, ntot, M, r, t, lg]) - 2 * (n1[Q, ntot, M, r, t, lg]) * lg)) *
  (Exp[σ31 * ((n3[Q, ntot, M, r, t, lg]) - 2 * (n1[Q, ntot, M, r, t, lg]) * 2 * lg] -
  1)
```

Our Intracavity Laser Intensity :

```
Ψ[Ipin_, ntot_, M_, r_, t_, lg_] :=
  - (h v21
    (-2 lg ntot σ21 (2 k32 M t21 (h v31 + t31 σ31 * (Q[Ipin, ntot, M, r, t, lg])) +
      eθ (h (v31 + k32 M t31 v31) + (1 - 2 k32 M t21) t31 σ31 *
        (Q[Ipin, ntot, M, r, t, lg])))) +
    (2 k32 M t21 (h v31 + 3 t31 σ31 * (Q[Ipin, ntot, M, r, t, lg])) +
      eθ (h (v31 + k32 M t31 v31) + (3 + 2 k32 M t21) t31 σ31 *
        (Q[Ipin, ntot, M, r, t, lg])))) Log[r t4])) /
  (2 t21 σ21
    (h k32 M t31 v31 +
      eθ (h (v31 + k32 M t31 v31) + 2 t31 σ31 * (Q[Ipin, ntot, M, r, t, lg]))))
  Log[r t4]))
```

Next we Define our Output Laser Intensity :

```
IIlase[Ipin_, ntot_, M_, r_, t_, lg_] :=
  Ψ[Ipin, ntot, M, r, t, lg] *
  (gth[r, t, lg] * lg * Exp[gth[r, t, lg] * lg] * t * (1 - r)) /
  ((Exp[gth[r, t, lg] * lg] - 1) * (1 + t2 * r * Exp[gth[r, t, lg] * lg]))
```

Rubricks for generating plots :

Omega Plots :

```
Plot[Q[Ipin, 1.85*1013, 9.66*1018, 0.2, 0.975, 2] , {Ipin, 0, 12000},  
GridLines → Automatic, Frame → True, PlotLabel → "Insert Title Here",  
FrameLabel → {"X-Axis Label" , "Y-Axis Label"}]
```

Laser Plots :

```
Plot[{IIlase[Ipin, ntot, 3.22*1018, r, t, lg] ,  
IIlase[Ipin, ntot, 6.44*1018, r, t, lg] ,  
IIlase[Ipin, ntot, 9.66*1018, r, t, lg] ,  
IIlase[Ipin, ntot, 1.28*1019, r, t, lg] ,  
IIlase[Ipin, ntot, 1.61*1019, r, t, lg]}, {Ipin, 0, 12000},  
GridLines → Automatic, Frame → True, PlotLabel → "Insert Title Here",  
FrameLabel → {"X-Axis Label" , "Y-Axis Label"}]
```

Part 3 : Frequency Dependent, Lasing

(Assume steady state)

Rate Equations ( $\Psi \neq 0$ )

$$\begin{aligned} \text{Solve} \left[ \right. & \\ & \left\{ 0 == \frac{-\Omega f}{h * v_{31}} + \sigma_{21} * (n_2 - n_1) * \frac{\Psi}{h * v_{21}} + \frac{n_2}{t_{21}} + \frac{n_3}{t_{31}}, \right. \\ & 0 == -\sigma_{21} * (n_2 - n_1) * \frac{\Psi}{h * v_{21}} + k_{32} * M * (n_3 - 2 * \text{Exp}[-\theta] * n_2) - \frac{n_2}{t_{21}}, \\ & 0 == n_1 + n_2 + n_3 - n_{\text{tot}}, \\ & \left. -\text{Log}[r * t^4] / (2 * l_g) == \sigma_{21} * (n_2 - n_1) \right\}, \\ & \{n_1, n_2, n_3, \Psi\} \left. \right] // \text{FullSimplify} \end{aligned}$$

Defining our state population densities and intracavity laser intensity :

$$\begin{aligned} n1[\Omega f\_ , n_{\text{tot}}\_ , M\_ , r\_ , t\_ , l_g] &:= \\ & (2 e^{\theta} l_g \sigma_{21} (h n_{\text{tot}} (1 + k_{32} M t_{31}) v_{31} - t_{31} \Omega f) + \\ & \quad h (2 k_{32} M t_{31} + e^{\theta} (1 + k_{32} M t_{31})) v_{31} \text{Log}[r t^4]) / \\ & (4 h l_g (k_{32} M t_{31} + e^{\theta} (1 + k_{32} M t_{31})) v_{31} \sigma_{21}) \\ n2[\Omega f\_ , n_{\text{tot}}\_ , M\_ , r\_ , t\_ , l_g] &:= \\ & (e^{\theta} (2 l_g \sigma_{21} (h n_{\text{tot}} (1 + k_{32} M t_{31}) v_{31} - t_{31} \Omega f) - h (1 + k_{32} M t_{31}) v_{31} \text{Log}[r t^4])) / \\ & (4 h l_g (k_{32} M t_{31} + e^{\theta} (1 + k_{32} M t_{31})) v_{31} \sigma_{21}) \\ n3[\Omega f\_ , n_{\text{tot}}\_ , M\_ , r\_ , t\_ , l_g] &:= \\ & (2 h k_{32} l_g M n_{\text{tot}} t_{31} v_{31} \sigma_{21} + 2 e^{\theta} l_g t_{31} \sigma_{21} \Omega f - h k_{32} M t_{31} v_{31} \text{Log}[r t^4]) / \\ & (2 e^{\theta} h l_g v_{31} \sigma_{21} + 2 h k_{32} l_g M t_{31} v_{31} \sigma_{21} + 2 e^{\theta} h k_{32} l_g M t_{31} v_{31} \sigma_{21}) \\ \Psi[I_{\text{pin}}\_ , n_{\text{tot}}\_ , M\_ , He\_ , r\_ , t\_ , l_g, \Delta v_{\text{pump}}] &:= \\ & - (v_{21} \\ & \quad (4 k_{32} l_g M t_{21} \sigma_{21} \\ & \quad \quad (-h n_{\text{tot}} v_{31} + t_{31} * (\Omega f[I_{\text{pin}}, n_{\text{tot}}, M, He, r, t, l_g, \Delta v_{\text{pump}}])) - \\ & \quad \quad 2 e^{\theta} l_g \sigma_{21} (h n_{\text{tot}} (1 + k_{32} M t_{31}) v_{31} - \\ & \quad \quad \quad (1 + 2 k_{32} M t_{21}) t_{31} * (\Omega f[I_{\text{pin}}, n_{\text{tot}}, M, He, r, t, l_g, \Delta v_{\text{pump}}])) + \\ & \quad \quad \quad h (2 k_{32} M t_{21} + e^{\theta} (1 + k_{32} M t_{31})) v_{31} \text{Log}[r t^4])) / \\ & (2 t_{21} (k_{32} M t_{31} + e^{\theta} (1 + k_{32} M t_{31})) v_{31} \sigma_{21} \text{Log}[r t^4]) \end{aligned}$$

```

System Parameters :

h := 6.626068 * 10-34

t21 :=

t31 :=

σ21 :=

σ31 :=

k32 :=

v31 :=

v21 :=

θ := 0.8670379156330899

gth[r_, t_, lg_] := -Log[r * t4] / (2 * lg)

k := 1.3806504 * 10-23

T :=

c := 3.0 * 1010

λ31 := c / v31

λ21 := c / v21

M :=

ntot :=

lg :=

r :=

t :=

γ := M * k32

```

Pressure Dependence of Absorption cross - section (courtesy Greg Pitz)

$$\Delta v_{31}[M, He] := \left( (((M) * k * T * (10^6) * (7.5006 * 10^{-3})) * 26.2) * 10^6) + \right. \\ \left. (((He) * k * T * (10^6) * (7.5006 * 10^{-3})) * 20.0) * 10^6) \right) * ((T / 310)^{(1/2)}) + 5.2 * 10^6$$

Cross - section and pump beam lineshapes :

$$f_{\text{pump}}[v, \Delta v_{\text{pump}}] := \left( \frac{2 * \text{Log}[2]^{1/2}}{\pi^{1/2} * \Delta v_{\text{pump}}} \right) * \text{Exp}[-4 * \text{Log}[2] * ((v - v_{31}) / \Delta v_{\text{pump}})^2]$$

$$\sigma\sigma_{31}[v, M, He] := \left( \frac{(\lambda_{31})^2}{8 * \pi * t_{31}} \right) * f_{31}[v, M, He]$$

$$f_{31}[v, M, He] := \left( \frac{1}{2 * \pi} \right) * \left( \frac{\Delta v_{31}[M, He]}{((v - v_{31})^2 + (\Delta v_{31}[M, He] / 2)^2)} \right)$$

Next We define our Input Beam Interaction with the system :

$$\Omega\Omega\Omega f[I_{\text{pin}}, \Omega f, n_{\text{tot}}, M, He, r, t, Lg, \Delta v_{\text{pump}}] := \\ \text{NIntegrate} \left[ \left( \frac{I_{\text{pin}} * f_{\text{pump}}[v, \Delta v_{\text{pump}}]}{Lg} \right) * \right. \\ \left. (1 - \right. \\ \left. \text{Exp} \left[ \right. \right. \\ \left. \left. (\sigma\sigma_{31}[v, M, He] * \right. \right. \\ \left. \left. (n_3[\Omega f, n_{\text{tot}}, M, r, t, Lg] - 2 * n_1[\Omega f, n_{\text{tot}}, M, r, t, Lg]) * 2 * Lg) \right] \right), \\ \left. \{v, v_{31} - 10^{11.5}, v_{31} + 10^{11.5}\} \right]$$

$$\Omega\Omega f[I_{\text{pin}}, n_{\text{tot}}, M, He, r, t, Lg, \Delta v_{\text{pump}}] := \\ (\Omega f /. \text{FindRoot}[\Omega\Omega\Omega f[I_{\text{pin}}, \Omega f, n_{\text{tot}}, M, He, r, t, Lg, \Delta v_{\text{pump}}] - \Omega f, \\ \{\Omega f, (I_{\text{pin}})\}])$$

Redefining our population densities as a function of  $I_{pin}$  :

```

nn1[Ipin_, ntot_, M_, He_, r_, t_, Lg_, Avpump_] :=
  (2 eθ Lg σ21
   (h ntot (1 + k32 M t31) v31 -
    t31 * (ΩΩf[Ipin, ntot, M, He, r, t, Lg, Avpump])) +
   h (2 k32 M t31 + eθ (1 + k32 M t31)) v31 Log[r t4]) /
  (4 h Lg (k32 M t31 + eθ (1 + k32 M t31)) v31 σ21)

nn2[Ipin_, ntot_, M_, He_, r_, t_, Lg_, Avpump_] :=
  (eθ
   (2 Lg σ21 (h ntot (1 + k32 M t31) v31 -
    t31 * (ΩΩf[Ipin, ntot, M, He, r, t, Lg, Avpump])) -
   h (1 + k32 M t31) v31 Log[r t4])) /
  (4 h Lg (k32 M t31 + eθ (1 + k32 M t31)) v31 σ21)

nn3[Ipin_, ntot_, M_, He_, r_, t_, Lg_, Avpump_] :=
  (2 h k32 Lg M ntot t31 v31 σ21 +
   2 eθ Lg t31 σ21 * (ΩΩf[Ipin, ntot, M, He, r, t, Lg, Avpump]) -
   h k32 M t31 v31 Log[r t4]) /
  (2 eθ h Lg v31 σ21 + 2 h k32 Lg M t31 v31 σ21 + 2 eθ h k32 Lg M t31 v31 σ21)

```

Finally our Laser Output as a function of our system parameters :

```

Iilase[Ipin_, ntot_, M_, He_, r_, t_, Lg_, Avpump_] :=
  (σ21 * (nn2[Ipin, ntot, M, He, r, t, Lg, Avpump] -
   nn1[Ipin, ntot, M, He, r, t, Lg, Avpump]) * Lg * t * (1 - r) *
   Exp[σ21 * (nn2[Ipin, ntot, M, He, r, t, Lg, Avpump] -
    nn1[Ipin, ntot, M, He, r, t, Lg, Avpump]) * Lg]) /
  ((Exp[σ21 * (nn2[Ipin, ntot, M, He, r, t, Lg, Avpump] -
   nn1[Ipin, ntot, M, He, r, t, Lg, Avpump]) * Lg] - 1) *
   (1 +
    t2 * r *
    Exp[σ21 * (nn2[Ipin, ntot, M, He, r, t, Lg, Avpump] -
     nn1[Ipin, ntot, M, He, r, t, Lg, Avpump]) * Lg])) *
  Ψ[Ipin, ntot, M, He, r, t, Lg, Avpump]

```

Rubrick for Generating Plots :

In this case it is suggested to create plots based on lists of data due to the high computational demands of evaluating the frequency dependent output beam intensity :

```
MultipleListPlot[
{Table[{Ipin, Ilase[Ipin, 1.85*1013, 9.66*1018, 1.61*1018, 0.2,
0.975, 2, 10*109]}, {Ipin, 0, 25000, 750}],
Table[{Ipin, Ilase[Ipin, 1.85*1013, 9.66*1018, 1.61*1018, 0.2,
0.975, 2, 50*109]}, {Ipin, 0, 25000, 750}],
Table[{Ipin, Ilase[Ipin, 1.85*1013, 9.66*1018, 1.61*1018, 0.2,
0.975, 2, 100*109]}, {Ipin, 0, 25000, 750}],
Table[{Ipin, Ilase[Ipin, 1.85*1013, 9.66*1018, 1.61*1018, 0.2,
0.975, 2, 200*109]}, {Ipin, 0, 25000, 750}],
Table[{Ipin, Ilase[Ipin, 1.85*1013, 9.66*1018, 1.61*1018, 0.2,
0.975, 2, 500*109]}, {Ipin, 0, 25000, 750}]], GridLines → Automatic,
Frame → True, PlotLabel → " Ilase vs Ipin (Frequency Dependent, Lasing)",
FillingStyle → None, PlotJoined → True,
FrameLabel → {"Ipin Watts/cm2", "Ilase Watts/cm2"},
PlotLegend → {10 GHz, 50 GHz, 100 GHz, 200 GHz, 500 GHz}]
```

#### Part 4 - Gamma Plots

Presented below is a complete algorithmic derivation for Gamma. In order to generate Gamma plots one must simply input the user parameters and execute the code below :

Defining Omega :

Single Frequency :

```

n1[Q_, ntot_, M_, He_, r_, t_, lg_] :=
  (2 h t31 v31 * (k32 * M) * Log[r t^4] +
   e^θ (h (v31 + t31 v31 * (k32 * M)) + t31 * (σ31) * Q) (2 lg ntot σ21 + Log[r t^4])) /
  (4 lg σ21 (h t31 v31 * (k32 * M) + e^θ (h (v31 + t31 v31 * (k32 * M)) + 2 t31 * (σ31) * Q)))

n2[Q_, ntot_, M_, He_, r_, t_, lg_] :=
  (e^θ (2 lg ntot σ21 (h (v31 + t31 v31 * (k32 * M)) + t31 * (σ31) * Q) -
   (h (v31 + t31 v31 * (k32 * M)) + 3 t31 * (σ31) * Q) Log[r t^4])) /
  (4 lg σ21 (h t31 v31 * (k32 * M) + e^θ (h (v31 + t31 v31 * (k32 * M)) + 2 t31 * (σ31) * Q)))

n3[Q_, ntot_, M_, He_, r_, t_, lg_] :=
  (t31 (2 lg ntot σ21 (h v31 * (k32 * M) + e^θ * (σ31) * Q) +
   (-h v31 * (k32 * M) + e^θ * (σ31) * Q) Log[r t^4])) /
  (2 lg σ21
   (h t31 v31 * (k32 * M) + e^θ (h (v31 + t31 v31 * (k32 * M)) + 2 t31 * (σ31) * Q)))

ΩΩΩ[Ipin_, Q_, ntot_, M_, He_, r_, t_, lg_] :=
  (Ipin / ((σ31) * (n3[Q_, ntot_, M_, He_, r_, t_, lg] - 2 * n1[Q_, ntot_, M_, He_, r_, t_, lg]) *
   lg)) *
  (Exp[(σ31) * (n3[Q_, ntot_, M_, He_, r_, t_, lg] - 2 * n1[Q_, ntot_, M_, He_, r_, t_, lg]) *
   2 * lg] - 1)

Ω1[Ipin_, ntot_, M_, He_, r_, t_, lg_] :=
  (Ωf /. FindRoot[ΩΩΩ[Ipin, Ωf, ntot, M, He, r, t, lg] - Ωf, {Ωf, (Ipin)}])

```



Broadband Case :

```

nb1[Qf_, ntot_, M_, r_, t_, Lg_] :=
  (2 eθ Lg σ21 (h ntot (1 + k32 M t31) v31 - t31 Qf) +
   h (2 k32 M t31 + eθ (1 + k32 M t31)) v31 Log[r t4]) /
  (4 h Lg (k32 M t31 + eθ (1 + k32 M t31)) v31 σ21)

nnb1[Ipin_, ntot_, M_, He_, r_, t_, Lg_, Δvpump_] :=
  (2 eθ Lg σ21
   (h ntot (1 + k32 M t31) v31 -
    t31 * (Qf[Ipin_, ntot_, M_, He_, r_, t_, Lg_, Δvpump_]))) +
   h (2 k32 M t31 + eθ (1 + k32 M t31)) v31 Log[r t4]) /
  (4 h Lg (k32 M t31 + eθ (1 + k32 M t31)) v31 σ21)

nb2[Qf_, ntot_, M_, r_, t_, Lg_] :=
  (eθ (2 Lg σ21 (h ntot (1 + k32 M t31) v31 - t31 Qf) - h (1 + k32 M t31) v31 Log[r t4])) /
  (4 h Lg (k32 M t31 + eθ (1 + k32 M t31)) v31 σ21)

nnb2[Ipin_, ntot_, M_, He_, r_, t_, Lg_, Δvpump_] :=
  (eθ
   (2 Lg σ21 (h ntot (1 + k32 M t31) v31 -
    t31 * (Qf[Ipin_, ntot_, M_, He_, r_, t_, Lg_, Δvpump_]))) -
   h (1 + k32 M t31) v31 Log[r t4])) /
  (4 h Lg (k32 M t31 + eθ (1 + k32 M t31)) v31 σ21)

nb3[Qf_, ntot_, M_, r_, t_, Lg_] :=
  (2 h k32 Lg M ntot t31 v31 σ21 + 2 eθ Lg t31 σ21 Qf - h k32 M t31 v31 Log[r t4]) /
  (2 eθ h Lg v31 σ21 + 2 h k32 Lg M t31 v31 σ21 + 2 eθ h k32 Lg M t31 v31 σ21)

nnb3[Ipin_, ntot_, M_, He_, r_, t_, Lg_, Δvpump_] :=
  (2 h k32 Lg M ntot t31 v31 σ21 +
   2 eθ Lg t31 σ21 * (Qf[Ipin_, ntot_, M_, He_, r_, t_, Lg_, Δvpump_] -
    h k32 M t31 v31 Log[r t4])) /
  (2 eθ h Lg v31 σ21 + 2 h k32 Lg M t31 v31 σ21 + 2 eθ h k32 Lg M t31 v31 σ21)

```

```

ΩΩΩf[Ipin_, Ωf_, ntot_, M_, He_, r_, t_, Lg_, Δvpump_] :=
NIntegrate[ $\left(\frac{Ipin * f_{pump}[v, \Delta vpump]}{Lg}\right) *$ 
(1 -
Exp[
(σσ31[v, M, He] *
(nb3[Ωf, ntot, M, r, t, Lg] - 2 * nb1[Ωf, ntot, M, r, t, Lg]) * 2 * Lg))],
{v, v31 - 1011.5, v31 + 1011.5}]

ΩΩf[Ipin_, ntot_, M_, He_, r_, t_, Lg_, Δvpump_] :=
(Ωf /. FindRoot[ΩΩΩf[Ipin, Ωf, ntot, M, He, r, t, Lg, Δvpump] - Ωf,
{Ωf, (Ipin)}])

ΩΩΩΩf[Ipin_, ntot_, M_, He_, r_, t_, Lg_, Δvpump_] :=
NIntegrate[
((Ipin * fpump[v, Δvpump]) /
(σσ31[v, M, He] * (nnb3[Ipin, ntot, M, He, r, t, Lg, Δvpump] -
2 * nnb1[Ipin, ntot, M, He, r, t, Lg, Δvpump]) * Lg)) *
(Exp[σσ31[v, M, He] *
(nnb3[Ipin, ntot, M, He, r, t, Lg, Δvpump] -
2 * nnb1[Ipin, ntot, M, He, r, t, Lg, Δvpump]) * 2 * Lg] - 1),
{v, v31 - 1011, v31 + 1011}]

Defining Gamma :

Γ[Ipin_, ntot_, M_, He_, r_, t_, Lg_, Δvpump_] :=
ΩΩΩΩf[Ipin, ntot, M, He, r, t, Lg, Δvpump] / Ω1[Ipin, ntot, M, He, r, t, Lg]

```

```

System Parameters :

h := 6.626068 * 10-34

t21 :=

t31 :=

σ21 :=

σ31 :=

k32 :=

v31 :=

v21 :=

θ := 0.8670379156330899

gth[r_, t_, lg_] := -Log[r * t4] / (2 * lg)

k := 1.3806504 * 10-23

T :=

c := 3.0 * 1010

λ31 := c / v31

λ21 := c / v21

M :=

ntot :=

lg :=

r :=

t :=

γ := M * k32

```

Pressure Dependence of Absorption cross - section (courtesy Greg Pitz)

$$\Delta v_{31}[M, He] := \left( (((M) * k * T * (10^6) * (7.5006 * 10^{-3})) * 26.2) * 10^6) + \right. \\ \left. (((He) * k * T * (10^6) * (7.5006 * 10^{-3})) * 20.0) * 10^6) \right) * ((T / 310)^{(1/2)}) + 5.2 * 10^6$$

Cross - section and pump beam lineshapes :

$$f_{\text{pump}}[v, \Delta v_{\text{pump}}] := \left( \frac{2 * \text{Log}[2]^{1/2}}{\pi^{1/2} * \Delta v_{\text{pump}}} \right) * \text{Exp}[-4 * \text{Log}[2] * ((v - v_{31}) / \Delta v_{\text{pump}})^2]$$

$$\sigma \sigma_{31}[v, M, He] := \left( \frac{(\lambda_{31})^2}{8 * \pi * t_{31}} \right) * f_{31}[v, M, He]$$

$$f_{31}[v, M, He] := \left( \frac{1}{2 * \pi} \right) * \left( \frac{\Delta v_{31}[M, He]}{((v - v_{31})^2 + (\Delta v_{31}[M, He] / 2)^2)} \right)$$

## Bibliography

1. ChemGlobe, 2000. <<http://www.chemglobe.org/>>
2. Hager, G.D., and G.P. Perram, "A three-level analytic model for alkali metal vapor lasers: part I. Narrowband optical pumping," *Applied Physics B*, (2010) DOI 10.1007/s00340-010-4050-6.
3. Hager, G.D., and G.P. Perram, "A three-level analytic model for alkali metal vapor lasers: part II. Solutions for Broad Band Optical Pumping," *Applied Physics B*, (2010) DOI 10.1007/s00340-010-4050-6.
4. Hecht, Jeff. "Back to the drawing board with Missile Beating Laser." *New Scientist*. 22 Feb. 2010 <<http://www.newscientist.com>>.
5. J. E. Sansonetti, J. Phys. Chem. Ref. Data **35**, 301–421 (2006); Erratum: **37**, 1183 (2008) DOI:[10.1063/1.2035727](https://doi.org/10.1063/1.2035727).
6. Krupke, W.F. *Diode-pumped alkali laser*, US Patent 6,643,311, 2003.
7. Krupke, William. "Diode-pumped alkali lasers aim for single-aperture power scaling" *SPIE Newsroom*. 2008.
8. Perschbacher *et al.* "High Efficiency Diode Pumped Rubidium Laser: Experimental Results." *XVI International Symposium on Gas Flow and Chemical Lasers and High Power Laser Conference*, Gmuden, Austria 29 January 2007.
9. Perram, Glen. "A New Approach for Tactical Laser Weapons: the Diode Pumped Alkali Laser." *AFIT/ENP* 2011.
10. Pitz, Greg *et al.* "Pressure Broadening of the D1 and D2 lines in Diode Pumped Alkali Laser." *Proceedings of SPIE Vol. 7005* 2008.
11. Pitz, G.A., C.V. Sulham, P. Jones, E.A. Acosta, and G.P. Perram, " Accepted: AIAA Plasmadynamics and Lasers Conference (2010).
12. Rodriguez, Mary. "Go With the Flow: Novel Diode-Pumped Alkali Laser Achieves First Light." *Air Force Print News*. 17 Dec. 2010 <<http://www.wpafb.af.mil/news>>.
13. Steck, Daniel. "Rubidium 87 D Line Data," available online at <http://steck.us/alkalidata> (revision 2.1.4, 23 December 2010).

14. Sulham *et al.* "A pulsed, optically pumped rubidium laser at high pump Intensity." *Optics Communications*, (2008).
15. Sulham, Cliff. "Laser Demonstration and Performance Characterization of Optically Pumped Alkali Laser System" *AFIT Dissertation* (2010).
16. Zamoski, N.D. *et al.* "A study of collisional quenching and radiation trapping kinetics for Rb(5p) in the presence of methane and ethane using time-resolved fluorescence." *Journal of Physics B* (2009) DOI 10.1088/0953-4075/42/24/245401.
17. Zweiback *et al.* "28W average power hydrocarbon-free rubidium diode pumped alkali laser." *Optics Express* (2010).

REPORT DOCUMENTATION PAGE				Form Approved OMB No. 074-0188	
<p>The public reporting burden for this collection of information is estimated to average 1 hour per response, including the time for reviewing instructions, searching existing data sources, gathering and maintaining the data needed, and completing and reviewing the collection of information. Send comments regarding this burden estimate or any other aspect of the collection of information, including suggestions for reducing this burden to Department of Defense, Washington Headquarters Services, Directorate for Information Operations and Reports (0704-0188), 1215 Jefferson Davis Highway, Suite 1204, Arlington, VA 22202-4302. Respondents should be aware that notwithstanding any other provision of law, no person shall be subject to a penalty for failing to comply with a collection of information if it does not display a currently valid OMB control number.</p> <p><b>PLEASE DO NOT RETURN YOUR FORM TO THE ABOVE ADDRESS.</b></p>					
1. REPORT DATE (DD-MM-YYYY) 24-03-2011		2. REPORT TYPE Master's Thesis		3. DATES COVERED (From – To) June 2008 – Mar 2011	
4. TITLE AND SUBTITLE  Broadband Pumping Effects on the Diode Pumped Alkali Laser				5a. CONTRACT NUMBER	
				5b. GRANT NUMBER	
				5c. PROGRAM ELEMENT NUMBER	
6. AUTHOR(S)  Paul Jones, Civilian				5d. PROJECT NUMBER	
				5e. TASK NUMBER	
				5f. WORK UNIT NUMBER	
7. PERFORMING ORGANIZATION NAMES(S) AND ADDRESS(S)  Air Force Institute of Technology Graduate School of Engineering and Management (AFIT/EN) 2950 Hobson Way WPAFB OH 45433-7765				8. PERFORMING ORGANIZATION REPORT NUMBER  AFIT/GAP/ENP/11-M04	
9. SPONSORING/MONITORING AGENCY NAME(S) AND ADDRESS(ES)  Brittany Edwards Southwestern Ohio Council for Higher Education 3155 Research Blvd., Suite 204 Dayton, OH 45420-4015				10. SPONSOR/MONITOR'S ACRONYM(S) SOCHE	
				11. SPONSOR/MONITOR'S REPORT NUMBER(S)	
12. DISTRIBUTION/AVAILABILITY STATEMENT APPROVED FOR PUBLIC RELEASE; DISTRIBUTION UNLIMITED					
13. SUPPLEMENTARY NOTES					
14. ABSTRACT This research seeks to gain greater insight on the mechanics of The Diode Pumped Alkali Laser through analytic modeling techniques. This work is an extension to a previous model developed by Dr. Gordon Hager, and focuses on the addition of pump-beam bandwidth. Specifically, it seeks to determine the effect that broadband pumping has on laser performance. The model incorporates all the fundamental parameters within the laser system, including alkali concentrations, collision partner concentrations, pump bandwidth, length and temperature of gain medium, transmission, and reflectivity. Baseline operating conditions set Rubidium (Rb) concentrations ranging from $10^{12}$ - $10^{14}$ atoms/cm <sup>3</sup> , corresponding to operating temperatures ranging from 50 – 150 C. Ethane or Methane concentrations are varied corresponding to partial pressures from 100 – 500 Torr. The system is evaluated for incident beam intensity ranging from 0 – 30000 W/cm <sup>2</sup> , for both lasing and non-lasing system analysis. Output laser beam intensities scale well with input beam intensity and the model predicts optical to optical efficiencies of over 70%.					
15. SUBJECT TERMS Diode Pumped Alkali Laser, gas laser, modeling, simulation, assessment tool					
16. SECURITY CLASSIFICATION OF:			17. LIMITATION OF ABSTRACT  UU	18. NUMBER OF PAGES 95	19a. NAME OF RESPONSIBLE PERSON Glen Perram, Ph.D. (AFIT/ENP)
a. REPORT	b. ABSTRACT	c. THIS PAGE			19b. TELEPHONE NUMBER (Include area code) 937-255-3636 x4504
U	U	U			

Standard Form 298 (Rev. 8-98)  
Prescribed by ANSI Std. Z39-18